

SAMPLE: Surface Structure Search Enabled by Coarse Graining and Statistical Learning

Lukas Hörmann, Andreas Jeindl, Alexander T. Egger, Michael Scherbela and Oliver T. Hofmann

Institute of Solid State Physics, NAWI Graz, Graz University of Technology, Petersgasse 16, 8010 Graz, Austria

Abstract

In this publication we introduce SAMPLE, a structure search approach for commensurate organic monolayers on inorganic substrates. Such monolayers often show rich polymorphism with diverse molecular arrangements in differently shaped unit cells. Determining the different commensurate polymorphs from first principles poses a major challenge due to the large number of possible molecular arrangements. To meet this challenge, SAMPLE employs coarse-grained modeling in combination with Bayesian linear regression to efficiently map the minima of the potential energy surface. In addition, it uses ab initio thermodynamics to generate phase diagrams. Using the example of naphthalene on Cu(111), we comprehensively explain the SAMPLE approach and demonstrate its capabilities by comparing the predicted with the experimentally observed polymorphs.

Keywords: Hybrid Organic/Inorganic Interface, Bayesian Linear Regression, Polymorphism, Surface Induced Phase, First Principles Simulation, Naphthalene on Cu(111)

1. Introduction

The principal information about a given solid material is arguably the particular polymorph it forms upon crystallization. Aside from its chemical composition, the structure of a material strongly influences its thermal[1], mechanical[2, 3], optical[4], and electronic[5] properties. The ability to predict the crystal structure therefore constitutes a powerful tool to gain insight into a material's properties without producing it. Of particular interest are hereby polymorphs that form at organic/inorganic interfaces, given their prevalence in technical applications.

Current approaches to structure search in general include minima hopping[6], basin hopping[7, 8], particle swarm optimization[9], (quasi-)random searches[10, 11], Bayesian learning[12, 13, 14, 15], genetic algorithms[16, 17, 18, 19, 20], neural networks[21], molecular dynamics[22], and stochastic optimization[23, 24, 25]. However, most of these methods only work well for free molecules or bulk crystals, with a few notable exceptions for interfaces[26, 27, 28, 29].

In this publication, we introduce the SAMPLE approach to surface structure search. SAMPLE stands

for *Surface Adsorbate Polymorph Prediction with Little Effort* and allows to efficiently predict polymorphs at organic/inorganic interfaces from first principles. In two previous publications[30, 31] we have already successfully applied parts of the SAMPLE approach. Here we present a comprehensive explanation and demonstration.

SAMPLE is a quasi-deterministic approach. This differentiates it from other structure search methods, such as basin hopping or genetic algorithms, which explore the potential energy surface stochastically. Additionally, SAMPLE provides a comprehensive overview over the relevant parts of the potential energy surface, including metastable configurations and defects. Moreover, SAMPLE can provide physical insight via the energies of the interactions between substrate and molecules as well as the molecule-molecule interactions[31].

The main challenge for any structure search method is the exponential increase of the number of polymorph candidates with the system's number of degrees of freedom. In fact, considering a continuous potential energy surface would lead to an infinite number of polymorph candidates. This circumstance is commonly referred to as configurational explosion.

To overcome said configurational explosion, SAMPLE employs an efficient and physically well-motivated coarse-grained model to discretize the potential energy surface. Within this model, a polymorph candidate corresponds to a particular arrangement of adsorbate molecules in a substrate supercell. Hereafter, we will use the term *configuration* to describe a polymorph candidate.

SAMPLE’s coarse-graining reduces the number of configurations to a finite, albeit large number. Evaluating their energies poses a conundrum: On the one hand, high accuracy is desired, since the energy of different polymorphs often differs by less than 20 meV[32, 33]. Such accuracies can only be provided by computationally expensive methods, such as dispersion-corrected DFT. On the other hand, calculating millions of energies requires computationally cheap methods, which are often rather inaccurate.

To resolve this conundrum, SAMPLE utilizes experimental design theory and Bayesian learning to predict the coarse-grained potential energy surface. Hence, SAMPLE only requires highly accurate calculations for a training set of a few hundred configurations to predict the remaining millions of configurations with the same accuracy as the underlying electronic structure theory. These energies can then be combined with ab initio thermodynamics to predict phase diagrams.

The paper is organized as follows: First, we discuss the key assumptions on which SAMPLE is based. Secondly, we describe the details regarding the coarse-grained modeling. Thirdly, we discuss the application of experimental design theory and Bayesian learning. Finally, we describe how we convert our results into phase diagrams using ab initio thermodynamics. Throughout the text, we illustrate the procedure on the example of naphthalene on Cu(111). Naphthalene is a small organic molecule, which forms a number of commensurate structures on the Cu(111) substrate depending on the preparation conditions[34, 35]. Hence, it is an ideal test system to demonstrate the capabilities of SAMPLE.

2. Basic Setup

SAMPLE gains its efficiency from coarse-graining the potential energy surface, which employs unit cells and local geometries as building blocks. In this section, we

discuss how these building blocks arise naturally for commensurate interfaces, and how they are implemented into the SAMPLE algorithm.

2.1. Commensurability as Key Premise and its Physical Implications

Calculating interface structures requires the use of periodic boundary conditions. These periodic boundary conditions need to account for periodicities of both, the substrate and the adsorbate. In other words, the adsorbate unit cells must be supercells of the substrate, i.e. the adsorbate layer must be *commensurate* with the substrate. At organic/inorganic interfaces, commensurability occurs under specific circumstances[36], which can be exploited to limit the search space. Specifically, commensurability implies that the interactions of the adsorbate molecules with the substrate are dominant compared to the interactions between the molecules. More precisely, the potential energy surface of molecules on the surface is sufficiently corrugated, such that molecule-molecule interactions cannot significantly displace or distort molecules. This is commonly observed and well justified for small, relatively rigid molecules[36], such as aromatic molecules, which are often used in organic electronics.

The implications of commensurability enable us to develop a coarse-grained model of the potential energy surface, as illustrated in figure 1. First, we generate substrate supercells which serve as unit cells of the adsorbate layer. Then, we can treat the local geometries as rigid building blocks and systematically place them into unit cells to assemble an exhaustive set of configurations. The geometries (see chapter 2.3) snap onto specific positions on the substrate (see figure 1). Within the coarse-grained model each configuration constitutes a point on the discretized potential energy surface.

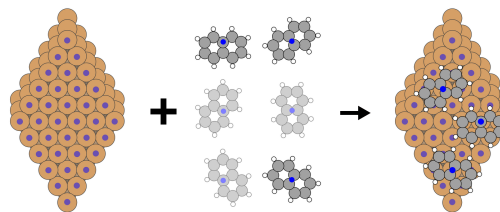


Figure 1: Schematic of building a configuration using a unit cell plus a number of local geometries.

2.2. The Standard Unit Cell

SAMPLE aims to generate all (symmetry-unique) unit cells within given constraints, such as unit cell area. However, a large set of equivalent unit cells can be generated via linear combinations of lattice vectors or symmetry transformations. Configurations that form in equivalent unit cells are identical and can, therefore, be removed from the pool of structures to be calculated. Defining a convention for standard unit cells allows us to identify symmetry-equivalent structures and facilitates comparison. In this section, we will describe the possible symmetry operations as well as the definition of this standard unit cells.

We can represent the unit cell of any ordered adsorbate layer in fractional coordinates of the primitive substrate lattice vectors by using an epitaxy matrix \mathbf{M} . The epitaxy matrix allows constructing the two-dimensional super-lattice vectors \mathbf{l}_1 and \mathbf{l}_2 of the unit cell from the primitive substrate lattice vectors \mathbf{v}_1 and \mathbf{v}_2 .

$$\begin{pmatrix} \mathbf{l}_1 \\ \mathbf{l}_2 \end{pmatrix} = \mathbf{M} \cdot \begin{pmatrix} \mathbf{v}_1 \\ \mathbf{v}_2 \end{pmatrix} = \begin{pmatrix} m_1 & m_2 \\ m_3 & m_4 \end{pmatrix} \cdot \begin{pmatrix} \mathbf{v}_1 \\ \mathbf{v}_2 \end{pmatrix} \quad (1)$$

In case of a commensurate configuration all elements m_1, m_2, m_3, m_4 of the epitaxy matrix are integer numbers.

In principle, for every unit cell an infinite number of equivalent cells exists. By defining a set of conclusive criteria, it is possible to select one of these equivalent unit cells as the *standard unit cell*. Such a standard unit cell not only allows identifying unique unit cells within the SAMPLE approach, but also to compare experimentally determined unit cells with those from SAMPLE. The criteria developed for the SAMPLE approach mainly enforce compact unit cells. We seek compactness in the oblique-angled fractional coordinates, rather than Cartesian coordinates. This allows working directly with epitaxy matrices. Compactness is ensured by minimizing the largest diagonal of the unit cell. Additionally, the standard unit cell should correspond to an epitaxy matrix that is as similar as possible to a diagonal matrix, i.e. it should have large diagonal and small off-diagonal elements. Further, we ensure that the standard unit cell has right-hand chirality, i.e. the determinant of the epitaxy matrix should be positive. A detailed discussion regarding the criteria for the standard unit cell can be found in chapter 4.1 of the supplementary information.

To find the standard unit cell we use two types of transformations: First, combinations of lattice vectors allow generating more compact unit cells. Secondly, symmetry transformations enable orienting the unit cell such that its epitaxy matrix becomes as similar as possible to a diagonal matrix. For better handling we employ fractional coordinates and can therefore directly combine and transform epitaxy matrices. Figure 2 illustrates the algorithm, which we explain in more detail below.

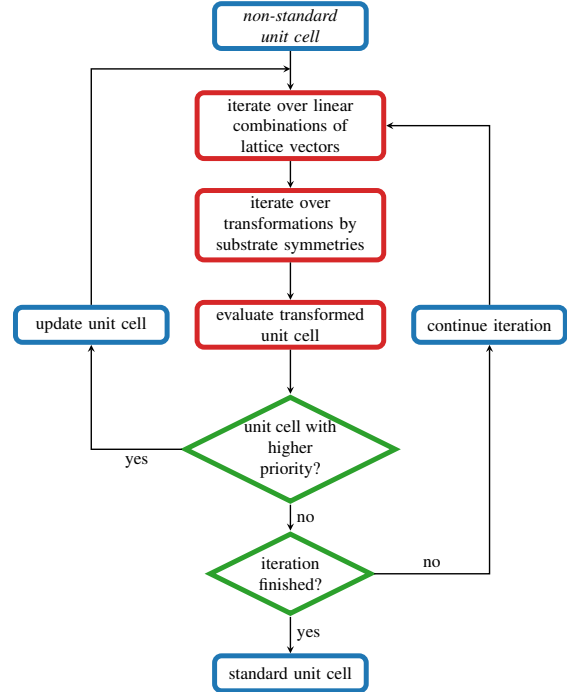


Figure 2: Flow diagram of the algorithm to determine the standard unit cell

2.2.1. Linear Combinations of Lattice Vectors

Combining the lattice vectors \mathbf{l}_1 and \mathbf{l}_2 of an original unit cell allows generating a new unit cell with the lattice vectors \mathbf{l}'_1 and \mathbf{l}'_2 .

$$\mathbf{l}'_1 = a\mathbf{l}_1 + b\mathbf{l}_2 \quad (2)$$

$$\mathbf{l}'_2 = c\mathbf{l}_1 + d\mathbf{l}_2 \quad (3)$$

The new and original unit cells are equivalent if the coefficients of this combination fulfill $a, b, c, d \in \mathbb{Z}$ and if the area of the unit cell is conserved. Combinations of lattice vectors allow transforming a unit cell into a more compact shape. For mathematical convenience,

we express the combination of lattice vectors (see equations 2 and 3) as a transformation of the epitaxy matrix:

$$\begin{pmatrix} m'_1 & m'_2 \\ m'_3 & m'_4 \end{pmatrix} = \underbrace{\begin{pmatrix} a & b \\ c & d \end{pmatrix}}_{\mathbf{T}} \cdot \begin{pmatrix} m_1 & m_2 \\ m_3 & m_4 \end{pmatrix} \quad (4)$$

In terms of lattice vectors, the parameters a, b, c, d denote how often a specific lattice vector is added. The parameters a and d elongate the unit cell, while b and c control the shear of the unit cell. To generate an equivalent unit cell, the transformation matrix \mathbf{T} must fulfill $|\det(\mathbf{T})| = 1$. A detailed discussion regarding the limits for the parameters a, b, c, d can be found in chapter 4.2 of the supplementary information.

2.2.2. Transformations by Substrate Point Group Symmetries

Multiplying the lattice vectors \mathbf{I}_1 and \mathbf{I}_2 with a symmetry matrix \mathbf{R} of the substrate transforms the unit cell into an equivalent unit cell with lattice vectors \mathbf{I}'_1 and \mathbf{I}'_2 . While such transformations do not change the compactness of the unit cell, they can yield epitaxy matrices that are more similar to a diagonal matrix.

$$\mathbf{I}'_1 = \mathbf{R} \cdot \mathbf{I}_1 \quad (5)$$

$$\mathbf{I}'_2 = \mathbf{R} \cdot \mathbf{I}_2 \quad (6)$$

2.2.3. Chirality

Two equivalent unit cells may also differ by the order of their epitaxy matrix elements. Switching the row in the epitaxy matrix flips the sign of the area. A unit cell with right-hand chirality has a positive area.

$$m_1 m_4 - m_2 m_3 > 0 \quad (7)$$

As shown in figure 2 we find the standard unit cell by iteratively applying linear combinations of lattice vectors and transformations by substrate symmetries. After each iteration step, we evaluate the priority of the transformed unit cell according to the above-specified criteria. If the new unit cell has a higher priority (better fulfills the criteria listed in chapter 4.1 of the supplementary information) we restart the iteration using the current transformed unit cell as input. In case the iteration finishes without finding a better unit cell, the current unit cell is the standard unit cell.

2.3. Local Geometries

The assumption of commensurability implies that inter-molecular interactions are not strong enough to expel adsorbate molecules from their local potential wells. It is therefore reasonable to expect that the geometry of an isolated molecule will not be significantly changed by the presence of other molecules, i.e. that the adsorption geometries of an isolated adsorbate molecule and a molecule in a close-packed adsorbate layer are similar.

We use the term *symmetry-inequivalent local geometry* to describe the atomic structure in which an isolated molecule adsorbs on a specific position on the substrate. Symmetry-inequivalent local geometries are energetically invariant under any symmetry operation of the substrate, such as rotation, mirroring or translation by primitive lattice vectors. Some symmetry operations map directly onto the original symmetry-inequivalent local geometry, while other symmetry operations generate an equivalent geometry with the same adsorption energy (see figure 3). Applying the different substrate point group symmetries to a symmetry-inequivalent local geometry allows building a set of symmetry-equivalent geometries, with identical adsorption energies. Hereafter we will use the term *local geometries* to encapsulate symmetry-inequivalent local geometries and their symmetry-equivalents and use them as building blocks to generate configurations. Since local geometries are invariant under translation by primitive lattice vectors, the substrate provides a natural discretization in form of the primitive substrate unit cells.

2.3.1. Local Geometries of Naphthalene on Cu(111)

To find the symmetry-inequivalent local geometries, we define a number of starting geometries that serve as starting points for local geometry optimizations. These optimization calculations then converge to a small number of distinct geometries, i.e. different starting geometries converge to the same final geometry. The FHI-aims quantum chemistry code (PBE + TS^{surf})[37, 38, 39] serves as our tool of choice to perform these calculations. Chapter 7 of the supplementary information contains a description of the employed settings.

For naphthalene on Cu(111) we find four symmetry-inequivalent local geometries with different

adsorption energies (see figure 3). The most favorable symmetry-inequivalent local geometry (fcc hollow) has an adsorption energy of -1.444 eV whereas the least favorable symmetry-inequivalent local geometry (bridge) has an adsorption energy of -1.365 eV . We find 3 local geometries for each symmetry-inequivalent local geometry, amounting to a total of 12 local geometries of naphthalene on Cu(111), as shown in figure 3.

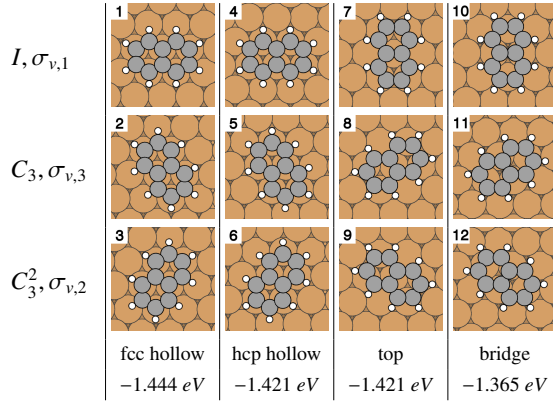


Figure 3: Local geometries for naphthalene on Cu(111). The column shows the symmetry operation used to obtain the geometries in the respective line from the geometries in the first line.

3. Generating Configurations

The integral goal of SAMPLE is to consider all possible molecular configurations in a given configuration space. The coarse-grained model SAMPLE is based upon presumes that adsorbates in close-packed configurations assume adsorption geometries that are similar to the local geometries. Because local geometries exist on the discrete grid of the primitive substrate lattice vectors, the number of configurations in a given unit cell is finite. This circumstance enables SAMPLE to investigate all configurations. Similar to the standard unit cell, we define a standard configuration which we obtain by combining a standard unit cell with a number of local geometries.

3.1. The Standard Configuration

As previously stressed, the main challenge for structure search results from the large number of possible configurations. Therefore, it would be desirable to represent configurations in an efficient and easily

comparable way. Since these requirements are reminiscent of the purpose hash functions have in computer science, it seems fitting to call such a representation configuration hash. In simple terms, the configuration hash is a one-to-one representation of a symmetry-unique configuration that incorporates the epitaxy matrix, the indices of local geometries and their positions. Grouped together, these three pieces of information constitute the configuration hash:

$$(m_1, m_2, m_3, m_4, g_1, g_2, \dots, g_n, p_1, p_2, \dots, p_n) \quad (8)$$

Here, m_1 thru m_4 are the elements of the epitaxy matrix, g_1 thru g_n are integers that represent the local geometries. In other words, we assign each local geometry a geometry index. The final elements, p_1 thru p_n , are the position indices of the respective geometries. We construct these position indices by systematically assigning every site on the substrate an index. Figure 4 illustrates how configuration and configuration hash relate to each other.

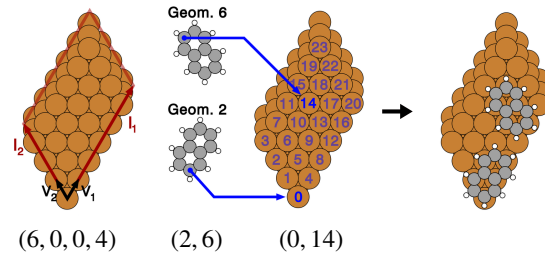


Figure 4: Example for the representation of a configuration in form of a tuple $(6, 0, 0, 4, 2, 6, 0, 14)$, whereby the elements $(6, 0, 0, 4)$ determine the unit cell, $(2, 6)$ constitute the local geometries and $(0, 14)$ their positions.

The most important function of the configuration hash is to identify symmetry-unique configurations. Different symmetry-equivalent configurations have different tuples in the form of equation (8). Because the configuration hash must be identical for equivalent configurations, we need to uniquely define one of these tuples as the configuration hash. We achieve this by defining an order relation for these tuples, which is similar to alphabetic ordering of words. For example: $(1, 5) < (5, 1)$. The smallest tuple is called configuration hash and the corresponding configuration is the standard configuration.

3.2. Combining Local Geometries and Unit Cells

The concept behind building a configuration is simple: We place a number of local geometries onto the discretization grid that spans the unit cell and prevent collisions between adsorbates. However, comprehensive structure search requires generating all possible configurations. The procedure illustrated in figure 5 allows generating configurations in a given unit cell and, which can trivially be repeated for each unit cell from chapter 2.2.

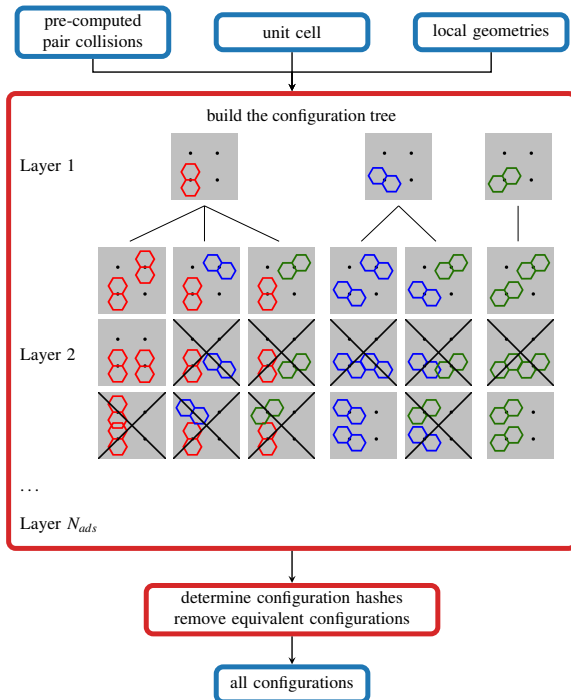


Figure 5: Flow diagram of the algorithm to generate configurations within one unit cell, repeating the procedure allows generating configurations for multiple unit cells

Generating configurations requires the definition of the unit cell, the number of local geometries that should be placed in it (and thereby the coverage) as well as the set of local geometries to chose from. Additionally, we define a set of distance thresholds d_0^{AB} , which determine the minimum distance between types of atoms belonging to different molecules. We define that two local geometries collide, if the distance between two respective atoms (of atom-type A and B) deceeds the distance threshold $d^{AB} < d_0^{AB}$ (see figure 9). This is to avoid the region of strong Pauli repulsion. Such configurations are high in energy and not relevant candidates for the global minimum.

The procedure for generating configurations comprises three main steps:

- Pre-compute all pair collisions: To improve efficiency, we predetermine a collision table containing pairs of local geometries and whether they collide. Therefore, we generate a list of all pairs of local geometries at specific distances (that fit into the unit cell). Using the distance threshold d_0^{AB} (see figure 9), allows determining which of these pairs collide.
- Build the configuration tree: The approach to systematically generate all configurations takes inspiration from tree diagrams. The first layer of the tree contains all configurations with one molecule per unit cell, the second layer all configurations with two molecules and so on. Since configurations are invariant under translations by a primitive substrate lattice vector, we place the first local geometry at the origin of the unit cell. For layer two, we add a second geometry to each configuration from layer one. Hereby, we place this second geometry onto every possible position of the unit cell and check for collisions using the collision table. Adding further layers follows the same principle. The total number of layers is equal to the number of molecules per unit cell N_{ads} .
- Remove symmetry-equivalent configurations: Finally, we convert all configurations into standard configurations and remove any duplicates.

This procedure allows SAMPLE to generate all configurations in a given unit cell. If we wish to generate all possible configurations for a given unit cell area, or a range of areas, we repeat the configuration generation for all corresponding unit cells.

3.3. Configurations for Naphthalene on Cu(111)

The commensurate polymorphs of naphthalene on Cu(111), that were found in experiment, exhibit coverages of $1.19 N_{ads}nm^{-2}$ to $1.48 N_{ads}nm^{-2}$ (15 to 12 primitive substrate unit cell areas A_{PUC} per naphthalene molecule) and have between 1 and 6 flat lying molecules per unit cell[34, 35]. For our structure prediction, we therefore select a slightly larger coverage range of 1.19 to $1.98 N_{ads}nm^{-2}$ (15 A_{PUC} to 9 A_{PUC} per naphthalene molecule) with 1 to 6 molecules per unit cell.

Since all outside atoms of naphthalene are H atoms, it is sufficient to define a single distance threshold d^{HH} . Here, we find that a distance of 0.15 nm (between twice the covalent and the van-der-Waals radius) provides an excellent compromise that allows to generate close-packed, but avoid an excessive number of high energy configurations.

While SAMPLE significantly pushes back the configurational explosion, we still eventually run into a proverbial configurational wall, as shown in figure 6. This prohibits exhaustively generating configurations with more than 4 molecules per unit cell. Requiring configurations to fulfill at least one symmetry operation of the substrate allows us to generate *high-symmetry* configurations with larger numbers of molecules. We generate about $43.6 \cdot 10^6$ configurations with 1 to 4 molecules per unit cell and, additionally, around $25 \cdot 10^4$ *high-symmetry* configurations with 5 and 6 molecules per unit cell. The configurational explosion requires us to limit the coverage range for 6 molecules to $1.37 N_{ads} \text{ nm}^{-2}$ to $1.98 N_{ads} \text{ nm}^{-2}$ ($13 A_{PUC}$ to $9 A_{PUC}$ per naphthalene molecule).

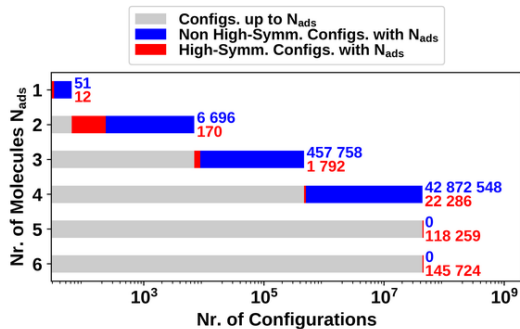


Figure 6: Number of configurations with increasing number of molecules per unit cell

4. Energy Determination

For the present example, SAMPLE's coarse-graining model generates a large number (in the order of 10^7) of possible configurations. Finding thermodynamically stable configurations requires ranking these possible configurations with respect to their adsorption energy or Gibbs free energy. The small differences in the adsorption energy of configurations necessitate high accuracy. However, directly calculating all adsorption

energies is unfeasible due to the large number of possible configurations.

To tackle this challenge, we employ Bayesian linear regression, which is based on a simple energy model and a number of physically motivated prior assumptions. Training the energy model with a small number of configurations, whose energies are calculated with dispersion-corrected DFT, allows predicting the energies of all generated configurations.

4.1. The Energy Model

The energy model takes its motivation from a series expansion of the adsorption energy of a configuration in terms of one-, two-, and many-body interactions. For our systems it is sufficient to consider one- and two-body interactions (see figure 7). This approach is somewhat reminiscent of cluster expansion. However, cluster expansion usually also considers three-, four- and further n-body interactions. Additionally, cluster expansion methods often assume that the effective cluster interaction coefficients are sparse, i.e. that only a small fraction of clusters is relevant for describing the property of interest (e.g. energy)[40]. Conversely, SAMPLE's energy model is not sparse. Considering all one and two-body contributions allows us not only to predict adsorption energies but also to extract physical insight from the energy model's coefficients.

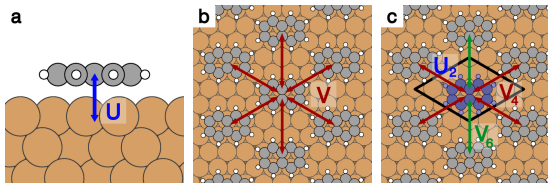


Figure 7: Components of the energy model: (a) one-body interactions, (b) two-body interactions (c) example of the energy model for a configuration with 1 molecule per unit cell

The one-body interactions are the interactions between the adsorbate at a specific adsorption site and the substrate. We note that one-body interactions are independent of the coverage, i.e. (de)polarization and similar effects are shifted onto the two-body terms. The two-body interactions take account of the energy contributions of individual pairs of local geometries. The discretization employed in SAMPLE guarantees that the number of different adsorbate pairs within a given distance cutoff is finite. The distance cutoff is

motivated by the fact that interaction energies between molecules decay to zero at large distances.

Using SAMPLE’s energy model, we can express the energy of a configuration as a sum of one-body interactions U_g and two-body interactions V_p , whereby n_g and n_p describe how often these interactions occur.

$$E_{config} = \sum_g n_g U_g + \sum_p n_p V_p \quad (9)$$

For the example in figure 7c E_{config} contains the one-body interaction term U_2 once and the two-body interaction terms V_4 and V_6 four and two times respectively. We divide the two-body interaction by two to account for double counting. For this example, we select a distance cutoff that only includes next nearest neighbors. Note that we usually also consider more distant pairs, which we neglect for this example for the sake of clarity. Using the energy model, the adsorption energy of this example in figure 7c is given by:

$$E_{config} = 1U_2 + 2V_4 + 1V_6 \quad (10)$$

Using equation (9) allows predicting the energies of all configurations, provided we know all one- and two-body interactions. However, it is difficult to calculate these model parameters directly. We could, for instance, use a large unit cell with periodic boundary conditions to find the one-body interaction of an isolated symmetry-inequivalent local geometry. This approach would, however, neglect collective effects, such as depolarization that results from a close-packed layer. Therefore, it would be desirable to calculate energies of close-packed configurations and infer the one- and two-body interactions. This way, the aforementioned effects would be implicitly included in the energy model.

We can use equation (9) to formulate a linear regression, which will bring us closer to the aforementioned goal. Therefore, we first rewrite equation (9) as a vector multiplication. Note that hereafter we will consider the adsorption energy per adsorbate molecules $E = E_{config}/N_{ads}$.

$$E = \frac{E_{config}}{N_{ads}} = \mathbf{n} \cdot \boldsymbol{\omega}^T \quad (11)$$

The model vector \mathbf{n} lists how often each one- or two-body interaction occurs in a given configuration. Hence, elements for one- and two-body interactions that are not

present in the configuration are zero. For one- and two-body interactions that do occur, the respective elements in \mathbf{n} consist of the number of occurrences divided by the number of molecules in the unit cell N_{ads} .

$$\mathbf{n} = \left(0, \dots, \frac{n_g}{N_{ads}}, 0, \dots, \frac{n_p}{N_{ads}}, 0, \dots \right) \quad (12)$$

For the example in figure 7c the model vector \mathbf{n} would contain three non-zero entries.

$$\mathbf{n} = \left(\underbrace{0, 1, 0, \dots}_{\text{one-body}}, \underbrace{0, 0, 0, 2, 0, 1, 0, \dots}_{\text{two-body}} \right) \quad (13)$$

The interaction vector $\boldsymbol{\omega}$ contains the energies assigned to the one- and two-body interactions.

$$\boldsymbol{\omega} = (U_1, U_2, \dots, V_1, V_2, \dots) \quad (14)$$

For a set of configurations, equation (9) becomes a matrix multiplication of a model matrix \mathbf{X} , whose lines are the vectors \mathbf{n} , and the interaction vector $\boldsymbol{\omega}$.

$$\mathbf{E} = \mathbf{X} \cdot \boldsymbol{\omega}^T \quad (15)$$

Having discussed its components, we can now formulate the aforementioned linear regression for the interaction vector $\boldsymbol{\omega}$. Hereby, it is necessary to allow for some flexibility in the fitting. To so do, we assume that the model energies \mathbf{E} can scatter around the actually calculated DFT energies \mathbf{E}_{DFT} for a set of configurations by a normal-distributed noise $\boldsymbol{\epsilon}$.

$$\mathbf{E}_{DFT} = \mathbf{E} + \boldsymbol{\epsilon} = \mathbf{X} \cdot \boldsymbol{\omega}^T + \boldsymbol{\epsilon} \quad \text{with } \boldsymbol{\epsilon} \sim \mathcal{N}(\mathbf{0}, \sigma_{model}^2 \mathbb{1}) \quad (16)$$

The noise $\boldsymbol{\epsilon}$ in equation 16 is determined by the model uncertainty σ_{model} . This is the inherent uncertainty between the energy model and the DFT calculations that remains even if the model is trained on an infinite number of DFT calculations. The number of elements in the interaction vector $\boldsymbol{\omega}$ (i.e., the total number of one- and two-body interactions) determines the dimensionality of the linear regression (see chapter 4.2.3). Calculating the energies of a small number of configurations \mathbf{E}_{DFT} and trying to find the least squares solution will however fail, if the system is under-determined. This is usually the case for the SAMPLE approach, since we typically use several 100 DFT calculations to determine several 1000 one- and two-body interactions. This is solved employing the framework of Bayesian linear regression.

4.2. Bayesian Linear Regression

Having formulated an energy model consisting of one- and two-body interactions, we now aim to determine these interactions with the aid of Bayesian linear regression, which is given by equation 17:

$$p(\omega|\mathbf{E}_{DFT}) = \frac{p(\mathbf{E}_{DFT}|\omega) p(\omega)}{p(\mathbf{E}_{DFT})} \quad (17)$$

Bayes' theorem enables expressing the unknown posterior probability for the one- and two-body interactions $p(\omega|\mathbf{E}_{DFT})$ in terms of two known probability distributions. These are the likelihood $p(\mathbf{E}_{DFT}|\omega)$ and the prior $p(\omega)$. In addition, the *marginal probability* $p(\mathbf{E}_{DFT})$ normalizes the posterior probability. Here the *marginal probability* is the probability to find DFT energies \mathbf{E}_{DFT} .

The likelihood is the probability to get \mathbf{E}_{DFT} given certain one- and two-body interactions ω . It directly follows from equation (16), whereby σ_{model} is the model uncertainty, i.e. the inherent uncertainty between the energy model and DFT.

$$p(\mathbf{E}_{DFT}|\omega) \propto \exp\left(-\frac{1}{2\sigma_{model}^2}\|\mathbf{E}_{DFT} - \mathbf{X}\omega\|^2\right) \quad (18)$$

The prior allows including physical knowledge about the system and thereby enables finding the expectation value for the one- and two-body interactions, even if the problem posed by equation 16 is under-determined. The prior covariance matrix C couples the parameters in ω and thereby reduces the number of independent parameters. We can write the prior as a normal distribution with the prior mean ω_0 and the prior covariance matrix C :

$$p(\omega) \propto \exp\left(-\frac{1}{2}(\omega - \omega_0)^T C^{-1}(\omega - \omega_0)\right) \quad (19)$$

Since both the likelihood and the prior are Gaussians, posterior probability is also a Gaussian. Further, the marginal probability $p(\mathbf{E}_{DFT})$ is taken to be constant and can therefore be neglected. Hence, we write the posterior probability as follows:

$$p(\omega|\mathbf{E}_{DFT}) \propto \exp\left(-\frac{1}{2}(\omega - \bar{\omega})^T C_{post}^{-1}(\omega - \bar{\omega})\right) \quad (20)$$

Here, the new posterior covariance matrix has the following expression:

$$C_{post}^{-1} = \frac{\mathbf{X}^T \mathbf{X}}{\sigma_{model}^2} + C^{-1} \quad (21)$$

The posterior mean $\bar{\omega}$ is also the expectation value for the interaction vector ω , which contains the one- and two-body interactions.

$$\bar{\omega} = C_{post} \left(\frac{\mathbf{X}^T \mathbf{E}_{DFT}}{\sigma_{model}^2} + C^{-1} \omega_0 \right) \quad (22)$$

Equation (22) is the best estimator for the interaction vector ω . To fit the energy model, we supply a set of configurations with energies from DFT and calculate the one- and two-body interactions. This in turn allows predicting the energies of all configurations.

4.2.1. Prior mean

The prior mean ω_0 takes account of the prior knowledge regarding the one- and two-body interactions. For the one-body interactions, the adsorption energy of a symmetry-inequivalent local geometry, i.e. an isolated molecule, provides a convenient estimator. Additionally, the one-body interaction uncertainty $\sigma_{one-body}$ controls how much a one-body interaction may differ from its prior.

Determining a prior mean for the two-body interactions is less straightforward. Since their energy contribution can either be attractive or repulsive, an obvious choice is starting with non-interacting geometries with a prior mean of zero.

In certain cases it is useful to employ SAMPLE in a two step approach and start with a two-body interaction prior from the interactions in the gas phase, rather than assuming non-interaction molecules on the surface. In this case, we first determine two-body interactions for the adsorbate layer in vacuum (using a non-interacting prior mean). Since the substrate requires the bulk of the computational effort of a DFT calculation, removing it allows generating a larger amount of data and consequently a good fit for the two-body interactions. We then use these two-body interactions for a molecule sheet in vacuum as prior mean for the adsorbed system. Such an approach works well for molecules with comparably strong molecule-molecule interactions, such as benzoquinone, which forms hydrogen bonds.

However, molecules on the substrate can experience charge transfer, leading to electrostatic repulsion and therefore significantly different interactions compared to a molecule sheet in vacuum. This is indeed the case for Naphthalene on Cu(111), where the work function of the adsorbate system is about 1 eV lower than that of

the clean Cu(111) slab. This work function shift indicates that the Naphthalene molecules become positively charged upon adsorption on the Cu substrate. Figure 8 shows a comparison of the performance of both prior means for naphthalene on Cu(111) and benzoquinone on Ag(111). For relevant training set sizes ($N_{set} > 60$) a gas phase prior mean does not improve the prediction for naphthalene, while we find significantly better predictions for benzoquinone. Increasing the number of training point leads to a convergence of the predictions with non-interacting prior mean and gas phase prior mean.

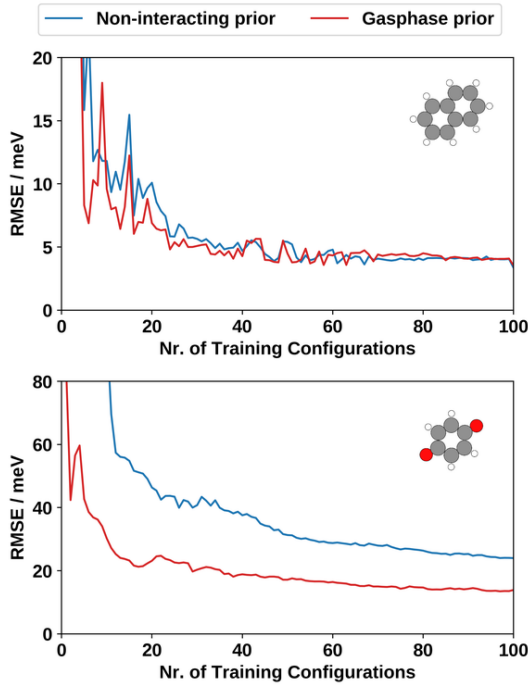


Figure 8: Dependence of the root mean square error of the predicted adsorption energies per molecule on the number of training configurations (see chapter 4.4) for non-interacting prior mean and gas phase prior mean. Top: Naphthalene on Cu(111). Bottom: Benzoquinone on Ag(111)

4.2.2. Prior covariance

The prior covariance enables including correlations between different interactions. The SAMPLE approach assumes no correlation between different one-body interactions or between one- and two-body interactions, but non-zero correlations between

different two-body interactions. The prior covariance for two-body interactions rests upon the assumption that similar pairs of geometries have similar two-body interactions. Note that similarity is not physically defined per se, but must be encoded via a (more or less) arbitrary feature vector (see chapter 4.3). Furthermore, the prior covariance is constructed in such a way that it converges to zero at large distances. In combination with the prior mean, this accounts for the assumption that the two-body interactions decays to zero at large distances. We use a multiplicative exponential kernel, which consists of two contributions:

- First, the distance in feature space $|f_i - f_j|$ provides a measure for the similarity between pairs, whereby f_i is the feature vector belonging to a specific pair of molecules. We also introduce the feature correlation length, which is used as a reference length to scale distances $|f_i - f_j|$ in the feature space. A large feature correlation length ξ entails non-disappearing correlation even for less similar pairs, while a small ξ restricts correlation to very similar pairs. In other words, if the feature distance $|f_i - f_j|$ is small compared to ξ , we assume similar two-body interactions for geometry pair i and geometry pair j . In case the feature distance is large compared to ξ , the two-body interactions may vary widely. Note that for one-body interactions only the C_{ii} are non-zero.

$$C_{ij} = \sigma_i^* \sigma_j^* \exp\left(-\frac{|f_i - f_j|}{\xi}\right) \quad (23)$$

- Second, we introduce a decay of the two-body interactions at large distances. This term depends on the minimum distance $d_{min,i}^{AB}$ between the atoms A-B of two geometries. Additionally, it includes the distance threshold d_0^{AB} and the real space decay length τ^{AB} for the pair atom species A-B. To attain a single value σ_i^* we take the arithmetic mean of the different atom-species pairs A-B. Note that other means may constitute an equally valid choice.

$$\sigma_i^* = \sigma_{two-body} \frac{1}{N_{AB}} \sum_{AB} \exp\left(-\frac{d_{min,i}^{AB} - d_0^{AB}}{\tau^{AB}}\right) \quad (24)$$

$\sigma_{two-body}$ is the standard deviation of the prior. The parameter τ^{AB} controls at which distance the two-body interactions converge to their prior mean ω_0 . A small τ^{AB} leads to a steeper decay to

the prior mean, while a large τ^{AB} leads to a slower decay. Given a fixed τ^{AB} , small distances between geometries ($|d_{min,i}^{AB} - d_0^{AB}| \ll \tau^{AB}$ with $d_{min,i}^{AB} - d_0^{AB} \geq 0$) result in a large σ_i^* , allowing for a larger difference between the two-body interactions and their prior mean. For large distances σ_i^* becomes small, allowing only for a small difference between interactions and prior mean.

4.2.3. Dimensionality of the Problem

The dimensionality of the problem at hand depends on the size of the interaction vector ω , which is given by the number of one- and two-body interactions. The number of one-body interactions is equal to the number of symmetry-inequivalent local geometries (four in case of naphthalene on Cu(111)). The number of two-body interactions depends, roughly speaking, on the number of (non-colliding) pairs. More precisely, it is determined by the distance cutoff and the settings for the feature vector (see chapter 4.3).

The prior covariance (see equation 23) defines a correlation between the two-body interactions. Hereby we may loosely differentiate between weakly and strongly correlated two-body interactions. While weakly correlated two-body interactions constitute essentially independent degrees of freedom, highly correlated two-body interactions do not increase the number of degrees of freedom.

In SAMPLE, the number of weakly correlated two-body interactions converges to a finite number. While changing the settings for the feature vector and increasing the distance cutoff allows to significantly increase the total number of two-body interactions, many of them are highly correlated.

Using more two-body interactions than necessary, while keeping otherwise similar settings, neither improves nor worsens the prediction accuracy (see chapter 6.6 in the supplementary information). Typical systems require several 1000 one- and two-body interactions.

In SAMPLE, the number of weakly correlated two-body interactions converges to a finite number. While the total number of two-body interactions depends on the precise settings of the feature vector (i.e., its dimensionality, the feature threshold, and the distance cutoff), increasing these values eventually only generate strongly correlated fit parameters.

While a large number can This can be seen by hypothetically increasing the distance cutoff τ . As can be seen from eq. WHATEVER, this may add additional two-body interactions, but these interaction are strongly correlated with interactions SOMETHING.

Since the number of weakly correlated two-body interactions is limited, increasing the dimensionality of the interaction vector will eventually only increase the number of highly correlated two-body interactions. Using more two-body interactions than necessary, while keeping otherwise similar settings, neither improves nor worsens the prediction accuracy (see chapter 6.6 in the supplementary information). Typical systems requires several 1000 one- and two-body interactions.

4.2.4. Hyperparameters

Bayesian linear regression requires a number of hyperparameters, namely the one-body interaction uncertainty $\sigma_{one-body}$, the two-body interaction uncertainty $\sigma_{two-body}$, the model uncertainty σ_{model} , the feature correlation length ξ , the real space decay length τ^{AB} and the distance cutoff d_{max}^{AB} .

The two-body interaction uncertainty $\sigma_{two-body}$ is the square root of the variance between prior mean and learned interaction energy. This hyperparameter should have a value in the range of the two-body interactions at molecule distances close to the distance threshold. For the model uncertainty σ_{model} we use the numerical DFT uncertainty, which we derived from the convergence criteria of our DFT settings. This is justified, since σ_{model} , which describes the scattering of the DFT energies around the energy model, is comparable to the numerical convergence of the DFT calculations.

We use a physically motivated settings for the real space decay length τ^{AB} and the distance cutoff d_{max}^{AB} . Additionally, chapter 6 of the supplementary information contains convergence plots for both parameters. We find that the root mean square error converges for $\tau \leq 0.5 \text{ nm}$ and for $d_{max} \leq 1 \text{ nm}$. While the distance cutoff does not enter into the equations, it controls which two-body interactions the model considers. The energy model only includes two-body interactions of molecule pairs if the smallest distance between their respective atoms is smaller than the distance cutoff d_{max}^{AB} (A and B being the atom species).

For the feature decay length ξ it is difficult to find physically motivated values. We determine ξ by minimizing the root mean square error for the naphthalene test system described in chapter 4.4 (details in chapter 6 in the supplementary information). The final settings we use for naphthalene on Cu(111) are summarized in table 1.

Table 1: Hyperparameter settings for Bayesian linear regression

parameter	symbol	setting
one-body interaction uncertainty	$\sigma_{one-body}$	100 meV
two-body interaction uncertainty	$\sigma_{two-body}$	100 meV
model uncertainty	σ_{model}	5 meV
feature correlation length	ξ	10
real space decay length	τ^{HH}	0.5 nm
distance cutoff	d_{max}^{HH}	1.6 nm

4.3. The Feature Vector

An integral part in SAMPLE's implementation of Bayesian linear regression is the feature vector. The feature vector acts as a descriptor for a pair of local geometries. Its main purpose is defining a measure of similarity between different geometry pairs. In general, the feature vector should be derived from the structure (not its properties) and it must be related to the property of interest. In other words, similar feature vectors should entail similar energies.

We construct the feature vector from the distances between the respective atoms of two local geometries. We differentiate between different atom species, since for instance, distances between H atoms relate differently to the adsorption energy than distances between C atoms. For naphthalene we can determine distances between H atoms, distances between H atoms and C atoms, as well as distances between C atoms. These different distances are shown in figure 9.

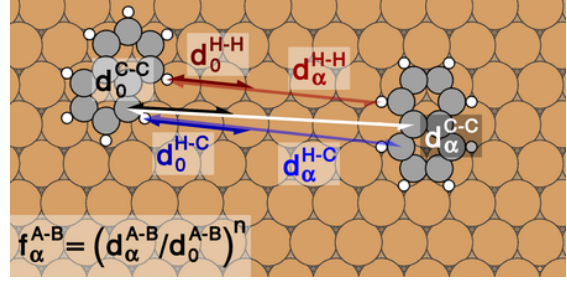


Figure 9: Example of the three possible types of distances and the respective distance thresholds for naphthalene molecules: between H atoms d_{α}^{HH} and d_0^{HH} , between H atoms and C atoms d_{α}^{CH} and d_0^{CH} , between C atoms d_{α}^{CC} and d_0^{CC} .

The feature vector itself consists of groups belonging to specific pairs A-B of atom species. A general feature vector for naphthalene would contain groups for H-H, H-C and C-C atom pairs. Note that for the specific example of naphthalene, distances between H atoms are sufficient.

$$\mathbf{f} = (f_1^{HH}, f_2^{HH}, \dots, f_1^{HC}, f_2^{HC}, \dots, f_1^{CC}, f_2^{CC}, \dots) \quad (25)$$

Each of these groups contains a number of feature vector elements f_{α} , which we calculate as follows:

$$f_{\alpha}^{AB} = \left(\frac{d_{\alpha}^{AB}}{d_0^{AB}} \right)^n \quad (26)$$

Here d_0^{AB} is the same distance threshold we used in chapter 3.2, d_{α}^{AB} is the distance between two atoms, and n is a negative decay power. The design of the feature vector is physically motivated. Since two-body interactions decay with distance (accounted for by the real space decay length, see equation 24), the energy contributions of close pairs vary more strongly with geometric differences than the small energy contributions of distant pairs. We account for this behavior by the negative decay power n . Hence, close pairs of molecules lead to large values in the feature vector, whereas distant pairs lead to small values. Therefore, small geometric differences of close molecule pairs entail large differences of the feature vectors and consequently less correlation. At the same time, features of distant molecule pairs show small variations.

Within each group AB the elements f_{α}^{AB} are arranged in descending order of their magnitude. Hence, the first element of each section represents the smallest distance between the atoms AB of this section. Since the

two-body interactions decay with distance, the first elements of the feature vector are most relevant for representing an interacting pair of molecules. For small molecules it is possible to use all distances. For larger molecules, we can reduce the dimension of the feature vector by truncating unimportant elements. To this aim, we define a feature dimension determining the number of elements in each section of the feature vector. Note that the dimensionality of the interaction vector only indirectly depends on the feature dimension and may not even change when increasing the feature dimension. The feature dimension should be as large as necessary for distinguishing between different pairs of molecules and as small as possible to limit computational effort. In case of two naphthalene molecules, there are 64 possible distances for H atoms alone. We show in chapter 6.5 of the supplementary information that a feature dimension of 16 already converges the root mean square error (RMSE).

Finally, we define a feature threshold Δf , which determines whether two feature vectors are similar. We consider two feature vectors \mathbf{f} and \mathbf{g} identical, if all individual elements differ by less than a feature threshold $|f_\alpha - g_\alpha| < \Delta f$. We note that different local geometry pairs can have the same feature vector.

4.3.1. The feature vector for Naphthalene

Since the outermost atoms of a flat-lying naphthalene molecule are the H atoms, it is sufficient to consider only distances between H atoms in the feature vector. Hence, we only require one distance threshold d_0^{HH} , which is the same as in chapter 3.3. In a pair of naphthalene molecules only 4 H atoms of one molecule can come close to 4 H atoms of the other molecule. Therefore, we use a feature dimension of 16, which accounts for all pair-wise distances between these $4 \cdot 4$ H atoms. Further, the decay power of $n = -2$ is inspired by the decay of Coulomb interactions. Finally, we find that a feature threshold $\Delta f = 0.01$ converges the root mean square error for the naphthalene test system described in chapter 4.4 (details in chapter 6 of the supplementary information). We demonstrate in chapter 4.6 that these settings yield excellent results. An overview of the parameter settings for the naphthalene feature vector is given in table 2.

4.4. Training Set Selection

Table 2: Hyperparameter settings for the naphthalene feature vector

parameter	symbol	setting
distance threshold	d_0	0.15 nm
feature threshold	Δf	0.01
feature dimension		16
decay power	n	-2

In order to determine the one- and two-body interactions, the Bayesian learning algorithm requires a set of training data. Naively, we could randomly select a number of configurations from all possible configurations. However, different training sets contain different amounts of information. For instance, a training set containing only configurations where the molecules are very close would yield accurate predictions for such closely packed configurations, but contain little information regarding loosely packed configurations. Hence, predictions for such configurations would be unreliable, making this training set unsuited for such a task.

A training set (see chapter 4.4) should contain as many different features as possible. Additionally, the unit cells in the training set should be as small as possible to minimize the computational effort. Conveniently, the two-molecule configurations already contain all combinations of two local geometries in all possible relative positions that fit into the unit cells. Hence, if d_{max} is sufficiently small, or the unit cells with two molecules are sufficiently large, the two-molecule configurations contain all possible molecule pairs and therefore all possible features.

The information contained in a training set is reflected by the posterior covariance matrix \mathbf{C}_{post} . In equation (20), the covariance matrix determines the uncertainty of the mean vector $\bar{\omega}$. Hence, minimizing \mathbf{C}_{post} will improve the accuracy of the fit coefficients. Since an order relation for matrices is not defined, minimizing \mathbf{C}_{post} cannot be done directly. Experimental design theory provides a number of optimality criteria for gauging the information contained in a matrix \mathbf{C}_{post} . The criterion chosen for SAMPLE is D-optimality[41]. D-optimality seeks to minimize the determinant of \mathbf{C}_{post} . More precisely, it minimizes the generalized variance of the fit parameters.

$$\min\{\det(\mathbf{C}_{post})\} \quad (27)$$

Equation (21) shows that the matrix \mathbf{C}_{post} consists of the model matrix \mathbf{X} and the prior covariance matrix \mathbf{C} .

Both matrices depend on the choice of the training set. Straightforwardly, we could evaluate $\det(\mathbf{C}_{post})$ for all possible training sets. This brute force approach would yield the global minimum of $\det(\mathbf{C}_{post})$, but poses a NP-hard problem[42]. Therefore, we use Fedorov’s algorithm[43] to approximate a D-optimal training set. Fedorov’s algorithm works in the following way: First we randomly select an initial training set with the desired number of configurations. Then, the algorithm iteratively tries to swap each configuration from the training set with every configuration from the pool of all configurations. A swap is accepted if it decreases the determinant of the covariance matrix $\det(\mathbf{C}_{post})$. Once the algorithm has tried all configurations from the pool and found the best swap, it proceeds to the next configuration from the training set. This process repeats itself until it no longer finds a better training set, i.e. could not swap any configuration. Fedorov’s algorithm allows limiting the computational cost of the selection while retaining SAMPLE’s quasi-deterministic nature.

4.5. D-optimal Selection Versus Random Selection

The simplest way to generate an unbiased set of training data is to randomly select training points. But this approach suffers from a lack of reproducibility. One training set might describe the system well, while another one performs poorly (see figure 10). Hence, several SAMPLE runs, with different random training sets, would be required to generate a reliable prediction. D-optimal selection solves this problem, since the minimum determinant $\min\{\det(\mathbf{C}_{post})\}$ is well defined. We demonstrate the advantage of D-optimal selection over random selection using two test systems: One for naphthalene on Cu(111), consisting of about 3200 configurations with 1 to 6 molecules per unit cell and one tetracyanoethylene on Cu(111) with about 1000 configurations with 1 to 2 upright standing molecules per unit cell. To reduce the computational effort, we strip the configurations of their metal substrates, i.e. we only consider naphthalene/tetracyanoethylene sheets in vacuum. This is justified for demonstrative purposes, since the symmetries of the system and therefore the correlation between feature distances and energy differences are retained. Figure 10 illustrates the improvement D-optimal selection provides over random selection. For relevant training set sizes ($N_{set} > 60$) D-optimal selection performs consistently better than random selection. Further, random training set selection leads

to differently performing training sets, while D-optimality produces consistent results.

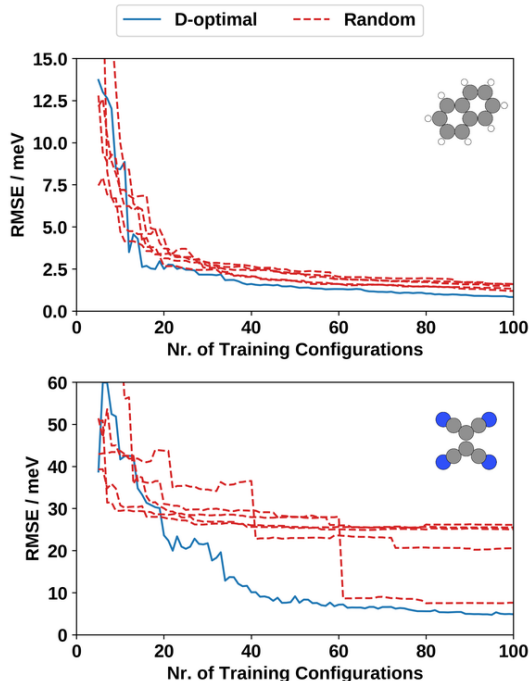


Figure 10: Dependence of the root mean square error of the predicted adsorption energies per molecule on the number of training configurations for D-optimal and random selection, (Top) Naphthalene test system, (Bottom) Tetracyanoethylene test system

4.6. Testing the Bayesian Linear Regression Algorithm

To test the Bayesian linear regression algorithm, we predict the adsorption energies of about $43.6 \cdot 10^6$ configurations as we have discussed in chapter 3.3. To determine the energy model we D-optimally select a training set of 259 configurations and calculate the adsorption energy with dispersion corrected DFT (PBE + TS^{surf})[37, 38, 39]. Using this model we are able to predict the adsorption energies of all configurations generated by the procedure discussed in chapter 3.3. To test the prediction, we randomly select 64 low energy configurations, which were not part of the training set, and calculate their adsorption energy with DFT. Comparing the latter with the predicted adsorption energies allows us to determine a RMSE. This measure acts as a quality criterion for our prediction. Figure 11 shows that there is excellent agreement between

predicted and the 64 calculated adsorption energies from the test set.

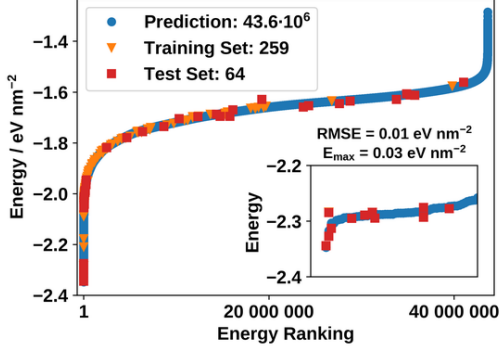


Figure 11: Predicted adsorption energy of naphthalene on Cu(111), training set: 259 D-optimally selected configurations, test set: 64 randomly selected configurations

We find a root mean square error of 0.01 eVnm^{-2} , which is smaller than the numerical DFT uncertainty (about 0.05 eVnm^{-2}). Additionally, this error is smaller than the often cited thermal energy scale $1 k_B T$, which corresponds to about 0.046 eVnm^{-2} for a coverage of $1.78 N_{ads} \text{ nm}^{-2}$ (10 Cu atoms per molecule).

5. Predicting Phase Diagrams

So far, we have discussed finding the coarse-grained potential energy surface using data from DFT calculations. By minimizing the adsorption energy, we can determine the most stable surface polymorph at 0 K . For experiments and technical applications, however, the interesting temperature range lies significantly above absolute zero. In addition, materials can form different polymorphs at different temperatures and pressures. These polymorphs can have vastly different physical properties and only specific polymorphs of a material may be suitable for a given application.

In thermodynamic equilibrium a closed system (that can exchange work and heat, but not matter with its surroundings) seeks to minimize the Gibbs free energy. At an interface the measure of interest is therefore the Gibbs free energy of adsorption γ . Therefore, the polymorph that forms at a certain temperature and pressure is the one with the lowest γ . To determine the Gibbs free energy of adsorption γ , we employ ab initio thermodynamics[44]. The Gibbs free energy γ is given

by equation 28. As commonly done in literature[44, 45, 46] we neglect the contributions of the vibration enthalpy, the configuration entropy and the mechanical work, which leads to:

$$\gamma = \frac{1}{A}(E - \mu_{ads}N_{ads}) \quad (28)$$

Here, E is the adsorption energy (the sum of one- and two-body interactions, see equation 11) as provided by SAMPLE. Further, N_{ads} is the number of adsorbates in the unit cell and μ_{ads} is the chemical potential of the adsorbate in the gas phase. The latter can be calculated by using the following approximation[44, 47]:

$$\mu_{ads} = \mu^{trans} + \mu^{rot} \quad (29)$$

The chemical potential of the adsorbate in the gas phase μ_{ads} consists of μ^{trans} , the translational and μ^{rot} , the rotational chemical potential. We neglect vibrational, electronic and nuclear contributions to μ_{ads} . First, consistency requires omitting the vibrational chemical potential, since we do not include the vibrational enthalpy for adsorbed molecules. Secondly, in most molecules electronic and nuclear excitation energies are large compared to $1 k_B T$. Hence, only the ground states, which we calculate with DFT, appreciably contribute to the chemical potential.[44] The equations for the translational μ^{trans} and rotational chemical potential μ^{rot} can be found in various textbooks such as the one by Cramer[47].

$$\mu^{trans}(p, T) = -k_B T \ln \left(\frac{(k_B T)^{5/2} (2\pi m)^{3/2}}{p h^3} \right) \quad (30)$$

The translational chemical potential μ^{trans} is a function of temperature T and pressure p . m is the mass of the molecule.

$$\mu^{rot}(T) = -k_B T \ln \left[\frac{\sqrt{\pi I_A I_B I_C} (8\pi^2 k_B T)^{3/2}}{\sigma h^3} \right] \quad (31)$$

The rotational chemical potential μ^{rot} , given here for a nonlinear molecule, is a function of temperature T . I_A, I_B, I_C are the different moments of inertia and σ is the symmetry number of the molecule. The latter is the

number of pure rotations that map the molecule onto itself.

The chemical potential is a property of the molecules in the gas phase and only depends on its temperature and pressure, making it the same for all configurations. Additionally, γ depends on the adsorption energy E and the area A of the unit cell (or the coverage). Hence, for a particular coverage, only the configuration with the lowest adsorption energy can show up in the phase diagram. This circumstance renders evaluating the Gibbs free energy of adsorption computationally inexpensive. This allows us to identify the configuration with the smallest γ for a range of temperatures and pressures and thereby generate a phase diagram.

5.1. Phase Diagram for Naphthalene on Cu(111)

We calculate the phase diagram for approximately $43.6 \cdot 10^6$ configurations as we have discussed in chapter 3.3. As depicted in figure 12, we observe seven different phases with a coverage ranging from $1.19 N_{ads}nm^{-2}$ to $1.78 N_{ads}nm^{-2}$ ($15 A_{PUC}$ to $10 A_{PUC}$ naphthalene molecule) and 2 thru 4 molecules per unit cell. The energetically most favorable configuration has 2 molecules per unit cell and a coverage of $1.78 N_{ads}nm^{-2}$ ($10 A_{PUC}$ per naphthalene molecule). This configuration also forms the phase with the highest packing density. configurations with higher coverage become less favorable in energy, due to the repulsion of the naphthalene molecules (see figure 13). The coverage decreases with decreasing pressure and increasing temperature. Further, if the temperature rises above roughly $300 K$ and the partial pressure of naphthalene drops roughly below $10^{-15} Pa$, it is no longer energetically favorable for naphthalene molecules to adsorb in the studied range of coverages.

In addition to the phase diagram, it is interesting to plot the adsorption energies of our $43.6 \cdot 10^6$ configurations against their individual coverages. Such an illustration, as depicted in figure 13, yields a quantitative comparison of all configurations.

In figure 13 the configurations with the lowest Gibbs free energies (at different temperatures and pressures) form a lower contour. In principle, all configurations within the energy uncertainty above this contour constitute equally valid phases. Therefore, it is interesting to take a look at these configurations and

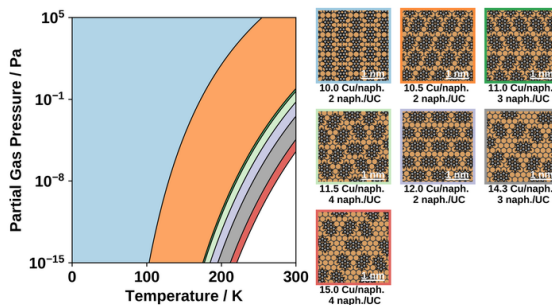


Figure 12: Phase diagram for naphthalene on Cu(111)

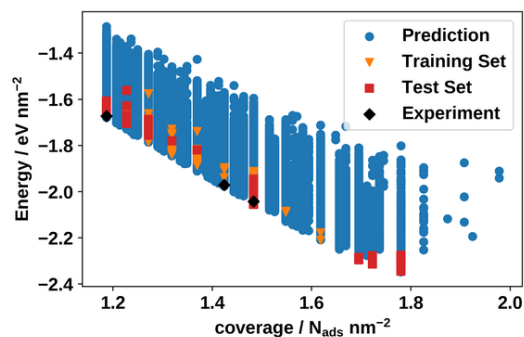


Figure 13: Plot of the adsorption energies against their individual coverages

figure out where the experimental configurations can be found in the prediction. Table 3 illustrates the experimental phases. We find that the predicted energies of the experimental configurations lie close to the lower contour, less than the numerical DFT uncertainty (about $0.05 eVnm^{-2}$) above the predicted lowest-energy configurations. Further we observe that the best adsorption energies per area decrease with increasing coverage until a coverage of $1.78 N_{ads}nm^{-2}$. Beyond this coverage, the best adsorption energies per area increase again.

Two experimentally determined phases have coverages that show up in the phase diagram, namely $1.48 N_{ads}nm^{-2}$ and $1.19 N_{ads}nm^{-2}$ ($12 A_{PUC}$ and $15 A_{PUC}$ per naphthalene molecule). Coverage $1.48 N_{ads}nm^{-2}$ corresponds to experimental phase (a) while coverage $1.19 N_{ads}nm^{-2}$ matches experimental phase (c) (see table 3). Both experimental phases contain 1 molecule per unit cell. A comparison between predicted and experimental configurations yields the following results:

- Experimental phase (a) matches a configuration whose predicted adsorption energy lies $(0.011 \pm 0.050) eVnm^{-2}$ higher than that of the best predicted configuration of equal coverage. The experimental configuration has rank 256 among configurations with coverage $1.48 N_{ads}nm^{-2}$.
- Experimental phase (b) has a coverage of $1.42 N_{ads}nm^{-2}$ (12.5 A_{PUC} per naphthalene molecule) and 6 molecules per unit cell. We find a matching configuration with an adsorption energy of $(0.005 \pm 0.050) eVnm^{-2}$ above the energetically most favorable configuration of the same coverage. Hence, the experimental configuration has rank 56 among configurations with coverage $1.42 N_{ads}nm^{-2}$.
- Experimental phase (c) matches the second best predicted configuration of equal coverage. The predicted adsorption energy of phase (c) is only negligibly higher ($0.0002 eVnm^{-2}$) than that of the best predicted configuration.

In all three cases the discrepancy is smaller than the numerical DFT uncertainty (about $0.05 eVnm^{-2}$). Further, the molecules adopt the fcc-hollow local geometry in all matching configurations. This is the energetically most favorable local geometry. Table 3 shows a summarized comparison between prediction and experiment.

6. Conclusion

In this publication we present SAMPLE, a comprehensive tool for surface structure search. SAMPLE is able to push back the configurational explosion by employing a coarse-grained model consisting of local geometries and unit cells. Furthermore, it makes use of optimal design theory in conjunction with a smart-data machine learning approach based on Bayesian linear regression. This allows for a quasi-deterministic exploration of the coarse-grained potential energy surface. SAMPLE requires only a small number of DFT calculations, serving as training data, to predict adsorption energies of millions of configurations. This capability gives SAMPLE a competitive edge over stochastic structure search methods. Beyond that, evaluating the prediction results with ab initio thermodynamics provides further insight into a system’s polymorphism.

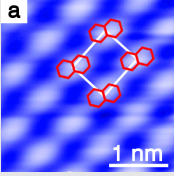
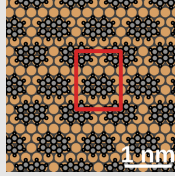
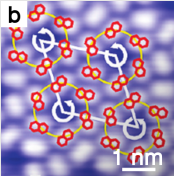
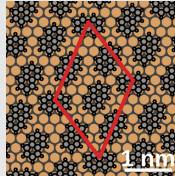
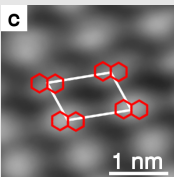
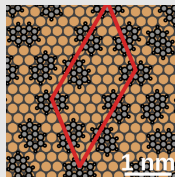
Experiment [34, 35]	Best Prediction per Coverage	$\Delta E / eVnm^{-2}$	Rank of
 $1.48 N_{ads}nm^{-2}$ 1 M/UC T=120 K	 $1.48 N_{ads}nm^{-2}$ 2 M/UC	0.011	257
 $1.42 N_{ads}nm^{-2}$ 6 M/UC T=120 K	 $1.42 N_{ads}nm^{-2}$ 4 M/UC	0.005	56
 $1.19 N_{ads}nm^{-2}$ 1 M/UC T=140 K	 $1.19 N_{ads}nm^{-2}$ 4 M/UC	0.0002	2

Table 3: Ranking of the experimental phases in our prediction: ΔE is the energy difference between experimental phases and lowest energy configuration of similar coverage, experimental figures modified with permission from [34, 35]

We demonstrate these capabilities using the example of naphthalene on Cu(111) and show SAMPLE’s ability to efficiently predict adsorption and Gibbs free energies of millions of possible commensurate configurations of molecules on surfaces. Moreover, the comparison with experiment demonstrates SAMPLE’s predictive power, since all experimental polymorphs rank within the numerical DFT uncertainty compared to the best prediction. Additionally, the phase diagram for naphthalene on Cu(111) yields an overview of the system’s behavior as function of the deposition conditions. SAMPLE achieves these results from first principles and without input of experimental parameters.

7. Acknowledgements

Financial support by Austrian Science Fund (FWF) project P28631-N36 and the START award Y 1157-N36 is gratefully acknowledged. Computational results have been achieved in part using the Vienna Scientific Cluster (VSC). An award of computer time was provided by the Innovative and Novel Computational Impact on Theory and Experiment (INCITE) program. This research used resources of the Argonne Leadership Computing Facility, which is a DOE Office of Science User Facility supported under Contract DE-AC02-06CH11357.

References

- [1] W. I. F. David, S. K. Callear, M. O. Jones, P. C. Aeberhard, S. D. Culligan, A. H. Pohl, S. R. Johnson, K. R. Ryan, J. E. Parker, P. P. Edwards, C. J. Nuttall, A. Amieiro-Fonseca, The structure, thermal properties and phase transformations of the cubic polymorph of magnesium tetrahydroborate, *Phys. Chem. Chem. Phys.* 14 (2012) 11800–11807.
- [2] C. Wang, S. Paul, K. Wang, S. Hu, C. C. Sun, Relationships among crystal structures, mechanical properties, and tableting performance probed using four salts of diphenhydramine, *Crystal Growth & Design* 17 (2017) 6030–6040.
- [3] P. Upadhyay, K. S. Khomane, L. Kumar, A. K. Bansal, Relationship between crystal structure and mechanical properties of ranitidine hydrochloride polymorphs, *CrystEngComm* 15 (2013) 3959–3964.
- [4] M. L. Tiago, J. E. Northrup, S. G. Louie, Ab initio calculation of the electronic and optical properties of solid pentacene, *Phys. Rev. B* 67 (2003) 115212.
- [5] C. Ambrosch-Draxl, D. Nabok, P. Puschnig, C. Meisenbichler, The role of polymorphism in organic thin films: oligoacenes investigated from first principles, *New Journal of Physics* 11 (2009) 125010.
- [6] S. Goedecker, Minima hopping: An efficient search method for the global minimum of the potential energy surface of complex molecular systems, *The Journal of chemical physics* 120 (2004) 9911–9917.
- [7] K. Krautgasser, C. Panosetti, D. Palagin, K. Reuter, R. J. Maurer, Global structure search for molecules on surfaces: Efficient sampling with curvilinear coordinates, *The Journal of chemical physics* 145 (2016) 084117.
- [8] D. J. Wales, J. P. Doye, Global optimization by basin-hopping and the lowest energy structures of lennard-jones clusters containing up to 110 atoms, *The Journal of Physical Chemistry A* 101 (1997) 5111–5116.
- [9] Y. Wang, J. Lv, L. Zhu, Y. Ma, Calypso: A method for crystal structure prediction, *Computer Physics Communications* 183 (2012) 2063–2070.
- [10] C. J. Pickard, R. Needs, Ab initio random structure searching, *Journal of Physics: Condensed Matter* 23 (2011) 053201.
- [11] D. H. Case, J. E. Campbell, P. J. Bygrave, G. M. Day, Convergence properties of crystal structure prediction by quasi-random sampling, *Journal of chemical theory and computation* 12 (2016) 910–924.
- [12] M. Todorović, M. U. Gutmann, J. Corander, P. Rinke, Efficient bayesian inference of atomistic structure in complex functional materials, *arXiv preprint arXiv:1708.09274* (2017).
- [13] D. M. Packwood, T. Hitosugi, Rapid prediction of molecule arrangements on metal surfaces via bayesian optimization, *Applied Physics Express* 10 (2017) 065502.
- [14] A. P. Bartók, M. C. Payne, R. Kondor, G. Csányi, Gaussian approximation potentials: The accuracy of quantum mechanics, without the electrons, *Physical review letters* 104 (2010) 136403.
- [15] Z. Li, J. R. Kermode, A. De Vita, Molecular dynamics with on-the-fly machine learning of quantum-mechanical forces, *Physical review letters* 114 (2015) 096405.
- [16] F. Curtis, X. Li, T. Rose, V. Vazquez-Mayagoitia, S. Bhattacharya, L. M. Ghiringhelli, N. Marom, Gator: A first-principles genetic algorithm for molecular crystal structure prediction, *Journal of Chemical Theory and Computation* 14 (2018) 2246–2264. PMID: 29481740.
- [17] R. L. Johnston, Evolving better nanoparticles: Genetic algorithms for optimising cluster geometries, *Dalton Transactions* (2003) 4193–4207.
- [18] M. Sierka, Synergy between theory and experiment in structure resolution of low-dimensional oxides, *Progress in Surface Science* 85 (2010) 398–434.
- [19] S. Heiles, R. L. Johnston, Global optimization of clusters using electronic structure methods, *International Journal of Quantum Chemistry* 113 (2013) 2091–2109.
- [20] M. dAvezac, A. Zunger, Identifying the minimum-energy atomic configuration on a lattice: Lamarckian twist on darwinian evolution, *Physical Review B* 78 (2008) 064102.
- [21] J. Behler, Representing potential energy surfaces by high-dimensional neural network potentials, *Journal of Physics: Condensed Matter* 26 (2014) 183001.
- [22] T.-Q. Yu, M. E. Tuckerman, Temperature-accelerated method for exploring polymorphism in molecular crystals based on free energy, *Phys. Rev. Lett.* 107 (2011) 015701.
- [23] E. Schneider, L. Vogt, M. E. Tuckerman, Exploring polymorphism of benzene and naphthalene with free energy based enhanced molecular dynamics, *Acta Crystallographica Section B* 72 (2016) 542–550.
- [24] R. L. Akkermans, N. A. Spenley, S. H. Robertson, Monte carlo methods in materials studio, *Molecular Simulation* 39 (2013) 1153–1164.
- [25] S. Kirkpatrick, C. D. Gelatt, M. P. Vecchi, Optimization by simulated annealing, *science* 220 (1983) 671–680.
- [26] G. Copie, Y. Makoudi, C. Krzeminski, F. Cherioux, F. Palmino, S. Lamare, B. Grandidier, F. Cleri, Atomic scale modeling of two-dimensional molecular self-assembly on a passivated si surface, *The Journal of Physical Chemistry C* 118 (2014) 12817–12825.
- [27] T. J. Roussel, E. Barrena, C. Ocal, J. Faraudo, Predicting supramolecular self-assembly on reconstructed metal surfaces, *Nanoscale* 6 (2014) 7991–8001.
- [28] G. Copie, F. Cleri, Y. Makoudi, C. Krzeminski, M. Berthe, F. Cherioux, F. Palmino, B. Grandidier, Surface-induced optimal packing of two-dimensional molecular networks, *Physical review letters* 114 (2015) 066101.
- [29] D. M. Packwood, P. Han, T. Hitosugi, Chemical and entropic control on the molecular self-assembly process, *Nature Communications* 8 (2017) 14463.
- [30] V. Obersteiner, M. Scherbela, L. Hörmann, D. Wegner, O. T. Hofmann, Structure prediction for surface-induced phases of organic monolayers: Overcoming the combinatorial bottleneck, *Nano Letters* 17 (2017) 4453–4460. PMID: 28640634.
- [31] M. Scherbela, L. Hörmann, A. Jeindl, V. Obersteiner, O. T. Hofmann, Charting the energy landscape of metal/organic interfaces via machine learning, *Phys. Rev. Materials* 2 (2018) 043803.

- [32] J. Bernstein, Polymorphism - a perspective, *Crystal Growth & Design* 11 (2011) 632–650.
- [33] J. Nyman, G. M. Day, Static and lattice vibrational energy differences between polymorphs, *CrystEngComm* 17 (2015) 5154–5165.
- [34] R. Forker, J. Peuker, M. Meissner, F. Sojka, T. Ueba, T. Yamada, H. S. Kato, T. Munakata, T. Fritz, The complex polymorphism and thermodynamic behavior of a seemingly simple system: Naphthalene on cu(111), *Langmuir* 30 (2014) 14163–14170. PMID: 25361739.
- [35] T. Yamada, M. Shibuta, Y. Ami, Y. Takano, A. Nonaka, K. Miyakubo, T. Munakata, Novel growth of naphthalene overlayer on cu(111) studied by stm, leed, and 2ppe, *The Journal of Physical Chemistry C* 114 (2010) 13334–13339.
- [36] D. E. Hooks, T. Fritz, M. D. Ward, Epitaxy and molecular organization on solid substrates, *Advanced Materials* 13 (2001) 227–241.
- [37] V. Blum, R. Gehrke, F. Hanke, P. Havu, V. Havu, X. Ren, K. Reuter, M. Scheffler, Ab initio molecular simulations with numeric atom-centered orbitals, *Computer Physics Communications* 180 (2009) 2175 – 2196.
- [38] J. P. Perdew, K. Burke, M. Ernzerhof, Generalized gradient approximation made simple, *Phys. Rev. Lett.* 77 (1996) 3865–3868.
- [39] V. G. Ruiz, W. Liu, E. Zojer, M. Scheffler, A. Tkatchenko, Density-functional theory with screened van der waals interactions for the modeling of hybrid inorganic-organic systems, *Phys. Rev. Lett.* 108 (2012) 146103.
- [40] A. H. Nguyen, C. W. Rosenbrock, C. S. Reese, G. L. Hart, Robustness of the cluster expansion: Assessing the roles of relaxation and numerical error, *Physical Review B* 96 (2017) 014107.
- [41] A. Wald, On the efficient design of statistical investigations, *Ann. Math. Statist.* 14 (1943) 134–140.
- [42] W. J. Welch, Algorithmic complexity: three np- hard problems in computational statistics, *Journal of Statistical Computation and Simulation* 15 (1982) 17–25.
- [43] A. C. Atkinson, The usefulness of optimum experimental designs, *Journal of the Royal Statistical Society. Series B (Methodological)* 58 (1996) 59–76.
- [44] J. Rogal, K. Reuter, Ab Initio Atomistic Thermodynamics for Surfaces: A Primer, RTO/NATO, pp. 2–1 – 2–18.
- [45] P. Herrmann, G. Heimel, Structure and stoichiometry prediction of surfaces reacting with multicomponent gases, *Advanced Materials* 27 (2015) 255–260.
- [46] K. Reuter, M. Scheffler, Composition, structure, and stability of ruo₂(110) as a function of oxygen pressure, *Phys. Rev. B* 65 (2001) 035406.
- [47] *Essentials of Computational Chemistry*, John Wiley & Sons, 2004.

Glossary

- A_{PUC}
primitive substrate unit cell area
- configuration
arrangement of local geometries in a unit cell
- configuration hash
unique representation of a configuration as a tuple of integer numbers
- decay power, n
hyperparameter representing the exponent of a feature vector element
- distance cutoff, d_{max}^{AB}
maximal distance between respective atom-species of two molecules, beyond which they become effectively non-interacting
- distance threshold, d_0^{AB}
minimal distance between respective atom-species of two molecules, below which strong Pauli repulsion occurs
- model uncertainty, σ_{model}
inherent uncertainty between the energy model and the DFT calculations, that remains even if the model is trained on an infinite number of DFT calculations
- E
adsorption energy of a configuration
- feature correlation length, ξ
hyperparameter influencing the similarity measure between two feature vectors
- feature dimension
number of elements in the feature vector
- feature threshold, Δf
distance in feature space that two feature vectors need to have in order to be distinct
- feature vector, f_i
representation of a pair of local geometries for Bayesian linear regression
- fractional coordinates
coordinates in fractions of the primitive substrate lattice vectors
- γ
Gibbs free energy of adsorption per area

interaction vector ω
vector containing all one- and two-body interactions

\mathbf{l}_i
unit cell lattice vector

likelihood
likelihood as defined in Bayes' theorem; here probability for the adsorption energies given the one- and two-body interactions

symmetry-inequivalent local geometry
adsorption geometry of an isolated molecule on the substrate

local geometry
symmetry-inequivalent local geometry or one of its symmetry-equivalents

M
epitaxy matrix

μ_{ads}
chemical potential of the molecules in gas phase

model matrix, \mathbf{X}
matrix consisting of several stacked model vectors

\mathbf{n}
model vector, \mathbf{n}
vector encoding which one- and two-body interactions occur in a configuration

N_{ads}
number of adsorbates per unit cell

numerical DFT uncertainty
uncertainty derived from the convergence of the DFT settings

one-body interaction, U_i
adsorption energy of a single local geometry

one-body interaction uncertainty, $\sigma_{one-body}$
standard deviation of the prior for one-body interaction

posterior probability
posterior probability as defined in Bayes' theorem; here probability for the one- and two-body interactions given the adsorption energies

posterior covariance, \mathbf{C}_{post}
covariance matrix of the Gaussian representing the posterior probability

posterior mean, $\bar{\omega}$
mean value of the Gaussian representing the posterior probability, best prediction for the one- and two-body interactions

prior
prior probability as defined in Bayes' theorem; here prior knowledge about the parameters of the energy model

prior covariance, \mathbf{C}
covariance matrix of the Gaussian representing the prior probability; prior knowledge about the correlations of different one- and two-body interactions in the energy model

prior mean, ω_0
mean value of the Gaussian representing the prior probability; prior knowledge about the one- and two-body interactions in the energy model

real space decay length, τ
hyperparameter controlling how quickly interactions decay with distance

standard unit cell
most compact representation of a unit cell

T
transformation matrix

two-body interaction, V_p
interaction energy between a pair of local geometries

two-body interaction uncertainty, $\sigma_{two-body}$
standard deviation of the prior for two-body interactions

\mathbf{v}_i
primitive substrate lattice vector

Supplementary Information

Lukas Hörmann, Andreas Jeindl, Alexander T. Egger, Michael Scherbela and Oliver T. Hofmann

Institute of Solid State Physics, NAWI Graz, Graz University of Technology, Petersgasse 16, 8010 Graz, Austria

1. Epitaxy Matrix and Types of Coincidence

In general, we can represent the unit cell of any ordered adsorbate layer in fractional coordinates of the primitive substrate lattice vectors (fractional coordinates). The transformation between Cartesian and fractional coordinates can be accomplished with an epitaxy matrix \mathbf{M} .

$$\begin{pmatrix} \mathbf{l}_1 \\ \mathbf{l}_2 \end{pmatrix} = \mathbf{M} \cdot \begin{pmatrix} \mathbf{v}_1 \\ \mathbf{v}_2 \end{pmatrix} = \begin{pmatrix} m_1 & m_2 \\ m_3 & m_4 \end{pmatrix} \cdot \begin{pmatrix} \mathbf{v}_1 \\ \mathbf{v}_2 \end{pmatrix} \quad (1)$$

Here \mathbf{l}_1 and \mathbf{l}_2 are the two-dimensional super-lattice vectors of the adsorbate unit cell, \mathbf{v}_1 and \mathbf{v}_2 are the primitive substrate lattice vectors and \mathbf{M} is the epitaxy matrix. Several types of epitaxy exist (see figure S1)[1]:

- (a) commensurability: All elements of the epitaxy matrix are integers $m_i \in \mathbb{Z}$ (see equation 1).
- (b) point-on-line coincidence: The adsorbate lattice lies on lines corresponding to the primitive substrate lattice.
- (c) coincidence II (or higher order commensurability): Only a fraction of the adsorbate lattice points coincide with the substrate, i.e. only the points of an adsorbate lattice supercell coincide.
- (d) incommensurability: The adsorbate lattice does not coincide with the substrate lattice or lattice lines thereof.

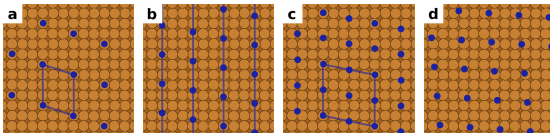


Figure S1: Types of epitaxy: (a) commensurability, (b) point-on-line coincidence, (c) coincidence II, (d) incommensurability

2. Geometric Considerations on Possible Configurations

In commensurate configurations, the smallest repeating unit contains only a small number of molecules. Even if we expand the definition to higher-order commensurate configurations, the number of molecules per unit cell still remains small. For instance, commensurate configurations of naphthalene on Cu(111) contain at most 6 molecules per unit cell[2, 3]. Hence, it is sensible to limit the number of molecules per unit cell and thereby limit the number of possible configurations.

Since close-packed configurations exhibit a large coverage $\Theta = N/A$ (number of molecules per area), we can enforce close-packing by introducing a maximum area for the possible adsorbate unit cells for a given number of molecules. Similarly, the fact that at least one molecule must fit in the unit cell provides a minimum area for the adsorbate unit cell. To avoid very elongated unit cells, we use the width of the adsorbate molecule as a lower boundary for the width of the unit cell. We enforce this criterion by a minimum unit cell width that is defined as the height of the parallelogram, formed by the super-lattice vectors (see figures S2 and S3).

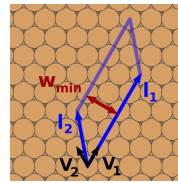


Figure S2: Parameters of a commensurate unit cell on a (111) surface: \mathbf{l}_1 , \mathbf{l}_2 are the lattice vectors of the unit cell and \mathbf{v}_1 , \mathbf{v}_2 are the primitive lattice vectors of the substrate, w_{min} is the minimum width of the unit cell

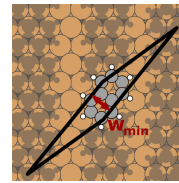


Figure S3: Example of an extremely elongated unit cell that is too narrow to accommodate a naphthalene molecule (w_{min} is too small)

Comprehensive structure search requires generating a set of all possible configurations that fulfill the aforementioned considerations. Within the SAMPLE approach, a configuration consists of a number of local adsorption geometries placed in a unit cell. Hence, the procedure to generate configurations necessitates comprehensive sets of unit cells as well as local adsorption geometries. Hereafter we will elaborate on the concepts employed in generating such a comprehensive set of configurations.

3. Calculation of the Largest Element of the Epitaxy Matrix

We propose epitaxy matrices by iterating over different values of the epitaxy matrix elements m_i . Generating all unit cells necessitates choosing limits for this iteration. Finding the limits requires some geometric considerations. The range within which we need to vary the matrix elements m_i depends on the largest super-lattice vector of a unit cell with a given area and a given minimum width. Using the area A and the minimum width w_{min} allows calculating the maximum length ℓ_{max} as follows:

$$\ell_{max} = \frac{A}{w_{min}} \quad (2)$$

We can also calculate ℓ_{max} by using the primitive lattice vectors \mathbf{v}_1 and \mathbf{v}_2 , as well as the epitaxy matrix elements m_1 and m_2 :

$$\ell_{max}^2 = (\mathbf{v}_1 m_1 + \mathbf{v}_2 m_2)^2 \quad (3)$$

We want to find the maximum values for m_1 and m_2 . To simplify the notation we define the unit cell vectors ℓ_1 and ℓ_2 as well as the cosine $\cos \alpha$ of the angle α between them.

$$\ell_1 = \mathbf{v}_1 m_1 \quad \ell_2 = \mathbf{v}_2 m_2 \quad \cos \alpha = \frac{\mathbf{v}_1 \mathbf{v}_2}{|\mathbf{v}_1| |\mathbf{v}_2|}$$

The law of cosines allows rewriting equation 3.

$$\ell_{max}^2 = \ell_1^2 + \ell_2^2 - 2\ell_1 \ell_2 \cos \alpha \quad (4)$$

Solving this for ℓ_1 gives:

$$\ell_1(\ell_2) = \ell_2 \cos \alpha \pm \sqrt{\ell_2^2 \cos^2 \alpha - \ell_2^2 + \ell_{max}^2} \quad (5)$$

To find the maximum of ℓ_1 , we need to take the derivative with respect to ℓ_2 and determine the roots.

$$\frac{d\ell_1}{d\ell_2} = \cos \alpha \pm \frac{1}{\sqrt{\dots}} \ell_2 (\cos^2 \alpha - 1) = 0 \quad (6)$$

We solve the above relation for ℓ_2 .

$$\ell_2 = \pm \left[\frac{\ell_{max}^2 \cos^2 \alpha}{1 - \cos^2 \alpha} \right]^{1/2} \quad (7)$$

Substituting ℓ_2 in equation 5 results in the expression for the maxima of $\ell_1(\ell_2)$. Equation 7 yields two solutions for ℓ_2 , a positive and a negative one. Hence, equation 5 has four solutions. We are only interested in the maximum absolute value $\ell_{1,max}$ of $\ell_1(\ell_2)$, which leads to the following expression. Due to symmetry, the solution for $\ell_2(\ell_1)$ is the same.

$$\ell_{1,max} = |\ell_2| |\cos \alpha| + \sqrt{\ell_2^2 \cos^2 \alpha - \ell_2^2 + \ell_{max}^2} \quad (8)$$

Now we calculate the maximum value that m_i can take round it to the next largest interger number.

$$m_1 = \left\lceil \frac{\ell_{1,max}}{|\mathbf{v}_1|} \right\rceil \quad (9)$$

$$m_2 = \left\lceil \frac{\ell_{1,max}}{|\mathbf{v}_2|} \right\rceil \quad (10)$$

$$m_{max} = \max(m_1, m_2) \quad (11)$$

In order to find all unit cells, we have to vary the elements m_i of the epitaxy matrix within a range given by m_{max} :

$$m_i \in [-m_{max}, m_{max}] \quad (12)$$

4. Algorithmic Details for the Standard Unit Cell

In principle, for every unit cell an infinite number of equivalent cells exist. However, by defining a set of conclusive criteria it is possible to select one of these equivalent unit cells as the standard unit cell. Transforming a unit cell into a standard unit cell requires two types of transformations: First, combinations of lattice vectors allow generating more compact unit cells and secondly, symmetry transformations enable orienting the unit cell such that it better fulfills the criteria for the standard unit cell.

4.1. Criteria for the Standard Unit Cell

To find a conclusive *standard unit cell* we require a number of criteria for the epitaxy matrix. These criteria are defined in hierarchical order, with criteria higher up in the hierarchy trumping the ones with lower priority. This avoids conflicts between criteria.

First, we minimize the larger diagonal of the unit cell. This criterion enforces compact unit cells.

1. $\min(d_{max}^2)$

Secondly, we compare elements of the epitaxy matrix. Criteria 2 thru 5 enforce that the epitaxy matrix is as close to a diagonal matrix as possible, i.e. the absolute value of the diagonal elements should be large, that of the off-diagonal elements should be small.

2. $|m_0| \geq |m_1|$
3. $|m_3| \geq |m_2|$
4. $|m_0| \geq |m_3|$
5. $|m_2| \geq |m_1|$

Thirdly, elements of the epitaxy matrix should be positive. These criteria favor unit cells that lie in the first quadrant.

6. $m_0 \geq 0$
7. $m_1 \geq 0$
8. $m_2 \geq 0$
9. $m_3 \geq 0$

If two unit cells fulfill criteria 1 thru 9, we pick the unit cell with the larger first element in the epitaxy matrix.

10. $\max(m_1)$

4.2. Parameters in the Transformation Matrix for the Standard Unit Cell

The first type of transformation, the combination of lattice vectors, is equivalent to a transformation of the epitaxy matrix. Hereby, equivalent unit cells can be obtained by using the transformation shown in equation 13, whereby the parameters of the transformation matrix T must fulfill $a, b, c, d \in \mathbb{Z}$ and $|\det T| = 1$:

$$\begin{pmatrix} m'_1 & m'_2 \\ m'_3 & m'_4 \end{pmatrix} = \underbrace{\begin{pmatrix} a & b \\ c & d \end{pmatrix}}_T \cdot \begin{pmatrix} m_1 & m_2 \\ m_3 & m_4 \end{pmatrix} \quad (13)$$

Finding useful limits for a, b, c, d will reduce the computational effort for finding the standard unit cell. Let us first consider the parameters a and d . If $b = c = 0$, the parameters a and d combine a lattice vector with itself. Setting $a = 1$ and $d = 1$ yields the original unit cell. Setting $a = 2$ or $d = 2$ doubles the length of the respective lattice vector and thereby doubles the area of the unit cell. Larger values of a and d increase the area even further, hence the upper limit is $a, d \leq 1$ ($b = c = 0$). Setting $a = -1$ or $d = -1$ subtracts the lattice vector twice from itself, reversing its direction. This is equivalent to a sign transformation. Hereby the area is conserved. However, larger negative values of a and d increase the area. Hence, the lower limit is $a, d \geq -1$. For a general case $b \neq 0$ and/or $c \neq 0$ this argument does not hold.

The parameters b and c control the shear of the transformed unit cell. If $a = d = 1$, any possible values of either b or c alter the direction of the respective lattice vector, but conserve the area of the unit cell. Conversely, varying both b and c at the same time may not conserve the area.

To find limits for the iteration of b and c , we remember that the standard unit cell should be as compact as possible. This means that its *shear* should be minimal. Therefore, we can use the shear of the current unit cell to calculate the limits for the iteration of b and c . We can calculate the shear as follows, whereby we round to the next larger integer since $a, b, c, d \in \mathbb{Z}$.

$$\begin{aligned} s_1 &= \lceil |\mathbf{l}_1 \mathbf{l}_2| / |\mathbf{l}_2|^2 \rceil \\ s_2 &= \lceil |\mathbf{l}_1 \mathbf{l}_2| / |\mathbf{l}_1|^2 \rceil \\ s_{max} &= \max(s_1, s_2) \end{aligned}$$

To guarantee finding the standard unit cell, we vary b and c within a range given by s_{max} .

$$b, c \in [-s_{max}, s_{max}] \quad (14)$$

4.3. Algorithm to Find for the Standard Unit Cell

In order to find the standard unit cell, we need to apply all combinations of a, b, c, d that are within the limits outlined in chapter 4.1 as well as all symmetry transformations included in the substrate's point-group. We can do so by iterating the parameters a, b, c, d and applying symmetry transformations. This is done in

five nested loops. The first four loops iterate a, b, c, d respectively while the fifth loop performs the symmetry transformations. Hereby, we enforce a conservation of the area. Figure S4 illustrates a number of examples for the transformation matrices T with the parameters a, b, c, d and the resulting unit cells, while figure S5 shows the effect of symmetry transformations.

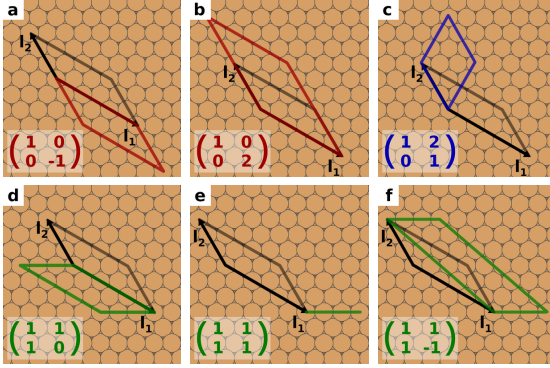


Figure S4: Examples of combining lattice vectors using a transformation matrix T : (a) transformation with $\det(T) = -1$ conserves the area, (b) $\det(T) = 2$ results in doubling the unit cell area and hence a non-equivalent unit cell, (c) shear through $b = 2$ conserves the area, (d) general valid transformation with $\det(T) = -1$, (e) if $\det(T) = 0$ the area becomes 0, (f) example with $\det(T) = 2$

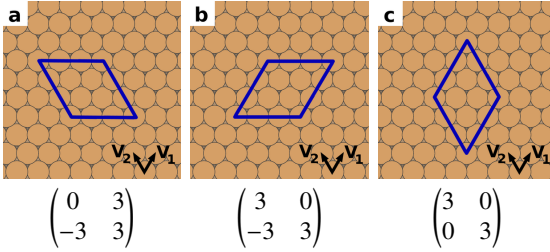


Figure S5: Examples of symmetry-equivalent unit cells: (a) epitaxy matrix with large non-diagonal elements, (b) epitaxy matrix fulfills criteria better than (a), (c) diagonal epitaxy matrix, which is the standard unit cell for this cell-shape

After every transformation, the unit cell is evaluated regarding the criteria for a standard unit cell. If the algorithm finds a unit cell that better fulfills the criteria, the iteration stops and the process of combining lattice vectors and applying symmetry transformations starts anew. If a loop ends without finding a better unit cell, the current unit cell is the standard unit cell.

5. Generating Unit Cells

In this chapter we aim to deliberate the technical aspects of generating unit cells according to the SAMPLE approach. As discussed in chapter 2, we intend to find close-packed commensurate configurations. This goal entails two considerations:

- The range of unit cell areas defines the possible coverages and number of molecule per unit cell.
- A minimum width of the unit cell should avoid generating narrow unit cells that cannot accommodate any molecules.

Usually, we are interested in unit cells of a given area. The area, given in units of the primitive substrate unit cell area A_{PUC} , directly relates to the epitaxy matrix via the following equation:

$$A = |m_1 m_4 - m_2 m_3| A_{PUC} \quad (15)$$

To generate possible unit cells, we iteratively propose different epitaxy matrices by varying the epitaxy matrix elements m_i . Using equation (15) we calculate the area of each proposed unit cell and only accept those with the desired area, i.e. we introduce an area constraint.

In order to find all possible unit cells, we require all combinations of the epitaxy matrix elements within a certain range $m_i \in [-m_{max}, m_{max}]$. A discussion on finding the maximal epitaxy matrix element m_{max} can be found in the supplementary information.

To systematically generate all aforementioned combinations, we can iterate the epitaxy matrix elements m_i with four nested loops, one for each element. Each loop starts the iteration at $m_i = -m_{max}$ and ends it at $m_i = m_{max}$. The computational effort of this task scales as $\mathcal{O}(m_{max}^4)$. However, using the area constraint reduces the number of independent epitaxy matrices elements m_i to three. The fourth m_i results automatically from equation (15). It is possible to reduce the computational effort to $\mathcal{O}(m_{max}^3)$, by considering three cases:

1. $m_1 \neq 0$
Equation 15 allows calculating the epitaxy matrix element m_4 directly.

$$m_4 = \frac{A + m_2 m_3}{m_1} \quad (16)$$

2. $m_1 = 0$ and $m_2 \neq 0$

In this case, the area is $A = m_2 m_3$ and m_4 becomes a free parameter. Hence, we calculate the value of m_3 and iterate m_4 within $[-m_{max}, m_{max}]$.

$$m_3 = A / m_2 \quad (17)$$

3. $m_1 = 0$ and $m_2 = 0$

The area is always 0.

Unit cells for naphthalene on Cu(111). For the example of naphthalene on Cu(111) the algorithm generates 987 unique unit cells with areas between 0.562 nm^2 (10 surface atoms) and 4.494 nm^2 (80 surface atoms). We set the minimum width to $w_{min} = 0.4 \text{ nm}$, slightly smaller than the naphthalene molecule.

6. Convergence Tests for Bayesian Linear Regression

To converge settings for SAMPLE's Bayesian linear regression algorithm, we use a test system of 3222 configurations whose metal substrates have been removed. The training set comprises 222 configurations. For the test set we use all 3222 configurations.

6.1. Feature Threshold

We determine the feature threshold using the test system described in this chapter. We calculate the root mean square error per molecule as well as the maximal error by predicting all 3222 configurations and comparing the results to the DFT calculations. We find that the root mean square error converges for a feature threshold of $\Delta f = 0.01$ and below (see figure S6). Since a smaller feature threshold reduces the computational effort we use a feature threshold of $\Delta f = 0.01$.

6.2. Feature Correlation Length

We determine the feature correlation length ξ using the same procedure as for the feature threshold. We find that the root mean square error converges for a feature correlation length between $\xi = 0.5$ and $\xi = 10$ (see figure S7). We use a feature correlation length of $\xi = 10$.

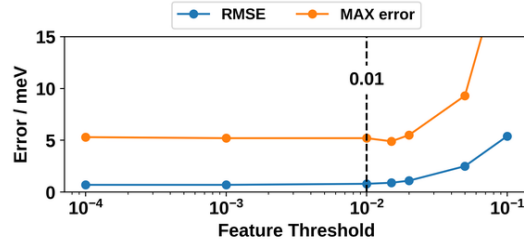


Figure S6: Convergence of the feature threshold

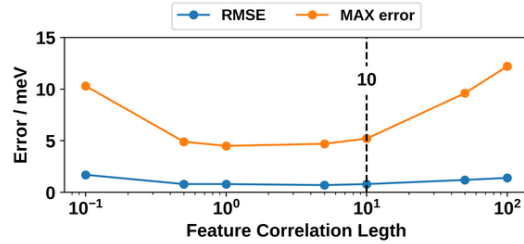


Figure S7: Convergence of the feature correlation length

6.3. Real Space Decay Length

We determine the real space decay length τ using the same procedure as for the feature threshold. We find that the root mean square error converges for a real space decay length above $\tau = 0.5 \text{ nm}$. Note that a large real space decay length effectively sets the coefficients σ_i^* to a constant.

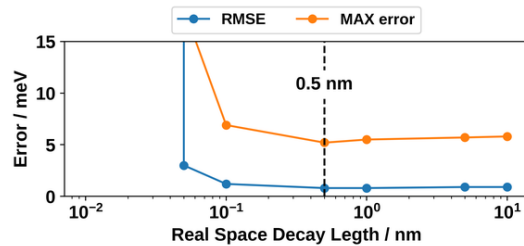


Figure S8: Convergence of the real space decay length

6.4. Distance Cutoff

We determine the distance cutoff d_{max} using the same procedure as for the feature threshold. The root mean square error converges for a distance cutoff above $d_{max} = 1 \text{ nm}$.

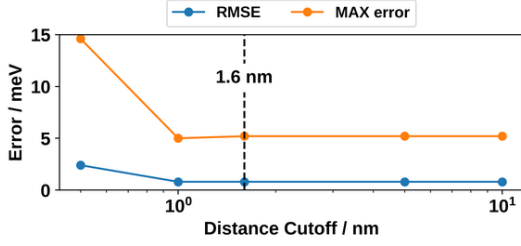


Figure S9: Convergence of the distance cutoff

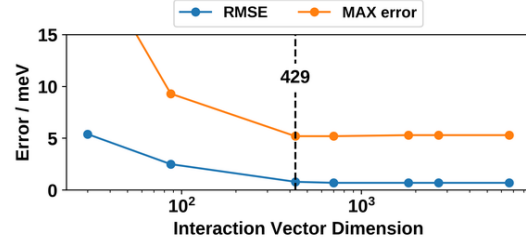


Figure S11: Convergence of the dimension of the interaction vector

6.5. Feature Dimension

We determine the feature dimension using the same procedure as for the feature threshold. The root mean square error converges for a feature dimension above 8.

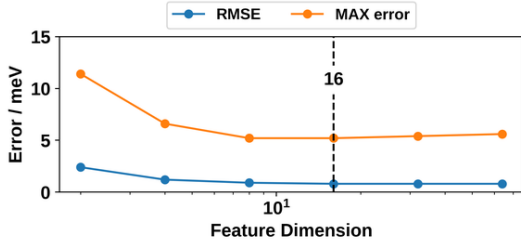


Figure S10: Convergence of the feature dimension

6.6. Dimensionality of the Interaction Vector

The dimensionality of the interaction vector is controlled by the distance threshold, the distance cutoff, the feature threshold, the decay power and the feature dimension. Here, we change the dimensionality by setting the distance cutoff to $d_{max} = 100 \text{ \AA}$ while varying the feature threshold. Training and test set are the same as for the convergence of the feature threshold. The root mean square error converges for a dimensionality of about 400 and above. We note that a large dimensionality significantly taxes computation resources, whereby the last data point in figure S11 requires about 15 min computation time (for the final parameter settings the computation time ranges in the seconds).

7. DFT Convergence Tests

7.1. Lattice Constant

The lattice constant is converged for a primitive fcc-bulk unit cell with a k-grid containing 80 k-points in each dimensions of the reciprocal unit cell (see figure S12). We find a lattice constant of 1.801 \AA , which is slightly smaller than the experimental lattice constant 1.808 \AA [4].

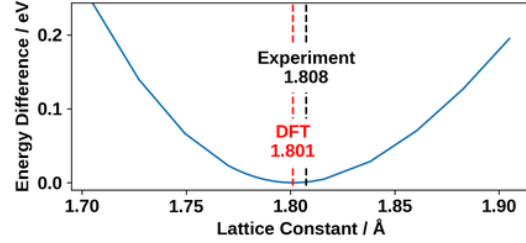


Figure S12: Lattice constant convergence

7.2. k-Grid

The k-grid is converged for a primitive fcc-bulk unit cell with a lattice constant of $a = 3.61 \text{ \AA}$ (see figure S13). We use the densest k-grid setting as reference. We select a k-point density equivalent to $80 \times 80 \times 80$ k-points for a primitive unit cell, resulting in an uncertainty of about 0.1 meV per Cu atom. Since we use 5 Cu layers for the substrate slab we get an uncertainty of 0.009 eVnm^{-2} (0.1 meV per single copper atom or 0.5 meV/Cu per surface atom in the 5 layer substrate).

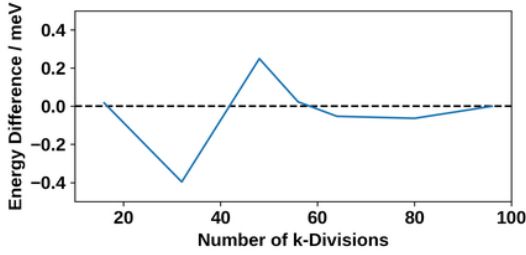


Figure S13: Convergence of the k-grid

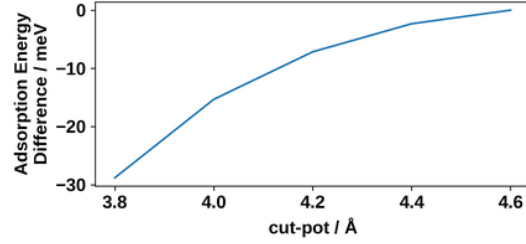


Figure S15: Convergence of the cut-pot onset

7.3. Number of Slab Layers

Using the repeated slab approach, we converge the number of substrate layers by considering the adsorption energy of a single naphthalene molecule in a (4, 0, 0, 4) unit cell (see figure S14). We use the seven layer slab as reference. The k-grid is set to 20 k-points in both horizontal directions (along the primitive lattice vectors) of the reciprocal unit cell and one k-point in the z-direction (perpendicular to the surface). We find that 5 Cu layers converge the uncertainty to about 0.018 eVnm^{-2} (16 meV per unit cell with 16 surface atoms).

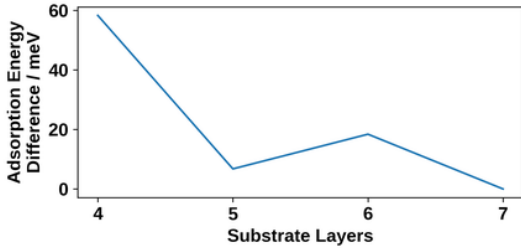


Figure S14: Layer convergence for slab

7.4. Onset of the cut-pot

The onset of the cutoff of the radial basis functions (first parameter of cut-pot) is converged using the adsorption energy of a single naphthalene molecule in a (4, 0, 0, 4) unit cell, with a k-grid containing 20 k-points in the lateral and 1 k-point in vertical directions (see figure S15). We use the largest cut-pot onset as reference. By setting the parameter cut-pot onset to 4.6 Å the calculation time is increased by +4 %, compared to the default setting. The remaining uncertainty is about 0.006 eVnm^{-2} (5 meV per unit cell with 16 surface atoms).

7.5. Removal of the 5g Basis Function for Cu

Removing the 5g basis function is tested using the adsorption energy of a single naphthalene molecule in a (4, 0, 0, 4) unit cell. The k-grid is set to 20 k-points in the x- and y-direction of the reciprocal unit cell and one k-point in the z-direction. We find a reduction in calculation time of 54 % and a resulting uncertainty of 0.017 eVnm^{-2} (0.01543 eV per unit cell with 16 surface atoms). Therefore, we use tier1 tight settings without the 5g basis function.

Adsorption Energy (tier1 tight)	-0.46273 eV
Adsorption Energy (tier1 tight without 5g)	-0.47816 eV
Difference	0.01543 eV

7.6. Radial Multiplier

Reducing the radial multiplier is tested using the adsorption energy of a single naphthalene molecule in a (4, 0, 0, 4) unit cell. The k-grid is set to 20 k-points in the x- and y-direction of the reciprocal unit cell and one k-point in the z-direction. Reducing the radial multiplier to 1 reduces the calculation time by 16 % and results in an uncertainty of 0.0015 eVnm^{-2} (0.00133 eV per unit cell with 16 surface atoms).

Adsorption Energy (Multiplier set to 2)	-0.46273 eV
Adsorption Energy (Multiplier set to 1)	-0.46406 eV
Difference	0.00133 eV

7.7. Additional DFT Settings

Apart from the aforementioned exceptions we use tier1 tight species settings. In addition, we use the following settings:

```
# General Settings:
xc pbe
```

```
spin none
charge 0
relativistic atomic_zora scalar
occupation_type gaussian 0.01
k_grid 20 20 1 # for a (4,0,0,4) unit cell

# Convergence Criteria:
sc_accuracy_forces 1e-3
sc_accuracy_rho 1e-2
sc_iter_limit 200
sc_accuracy_etot 1e-5

# Other Settings:
collect_eigenvectors .false.
RI_method lvl_fast
vdw_correction_hirshfeld .true.
compensate_multipole_errors .true.
use_dipole_correction .true.
```

References

- [1] D. E. Hooks, T. Fritz, M. D. Ward, Epitaxy and molecular organization on solid substrates, *Advanced Materials* 13 (2001) 227–241.
- [2] R. Forker, J. Peuker, M. Meissner, F. Sojka, T. Ueba, T. Yamada, H. S. Kato, T. Munakata, T. Fritz, The complex polymorphism and thermodynamic behavior of a seemingly simple system: Naphthalene on cu(111), *Langmuir* 30 (2014) 14163–14170. PMID: 25361739.
- [3] T. Yamada, M. Shibuta, Y. Ami, Y. Takano, A. Nonaka, K. Miyakubo, T. Munakata, Novel growth of naphthalene overlayer on cu(111) studied by stm, leed, and 2ppe, *The Journal of Physical Chemistry C* 114 (2010) 13334–13339.
- [4] R. Wyckoff, Interscience publishers, new york, new york rocksalt structure, *Crystal structures* 1 (1963) 85–237.